

1

Abstract

2

# Measurement of total hadronic differential cross sections in the LArIAT experiment

3

4

Elena Gramellini

5

2018

6

Abstract goes here. Limit 750 words.

7 **Measurement of total hadronic differential**  
8 **cross sections in the LArIAT experiment**

9 A Dissertation  
10 Presented to the Faculty of the Graduate School  
11 of  
12 Yale University  
13 in Candidacy for the Degree of  
14 Doctor of Philosophy

15 by  
16 Elena Gramellini

17 Dissertation Director: Bonnie T. Fleming

18 Date you'll receive your degree



21

*A mia mamma e mio babbo,*

22

*grazie per le radici e grazie per le ali.*

23

*To my mom and dad,*

24

*thank you for the roots and thank you for the wings.*

# Contents

25		
26	<b>Acknowledgements</b>	<b>vi</b>
27	<b>0 Total Hadronic Cross Section Measurement Methodology</b>	<b>1</b>
28	0.1 Event Selection . . . . .	2
29	0.1.1 Selection of Beamline Events . . . . .	2
30	0.1.2 Particle Identification in the Beamline . . . . .	3
31	0.1.3 TPC Selection: Halo Mitigation . . . . .	3
32	0.1.4 TPC Selection: Shower Removal . . . . .	4
33	0.2 Beamline and TPC Handshake: the Wire Chamber to TPC Match . .	5
34	0.3 The Thin Slice Method . . . . .	7
35	0.3.1 Cross Sections on Thin Target . . . . .	7
36	0.3.2 Not-so-Thin Target: Slicing the Argon . . . . .	8
37	0.3.3 Corrections to the Raw Cross Section . . . . .	10
38	0.4 Procedure testing with truth quantities . . . . .	11
39	<b>1 Preparatory Work</b>	<b>13</b>
40	1.1 Cross Section Analyses Data Set . . . . .	13
41	1.2 Construction of a Monte Carlo Simulation for LArIAT . . . . .	15
42	1.2.1 G4Beamline . . . . .	15
43	1.2.2 Data Driven MC . . . . .	19
44	1.2.3 Estimate of Energy Loss before the TPC . . . . .	22

45	1.3	Tracking Studies . . . . .	25
46	1.3.1	Study of WC to TPC Match . . . . .	26
47	1.3.2	Tracking Optimization . . . . .	29
48	1.3.3	Angular Resolution . . . . .	29
49	1.4	Energy Calibration and Studies . . . . .	33
50	1.4.1	Energy Calibration . . . . .	33
51	1.4.2	Uncertainty on Kinetic Energy . . . . .	33
52	1.4.3	dE/dX . . . . .	36
53	1.4.4	Energy Deposited . . . . .	37
54	<b>2</b>	<b>Negative Pion Cross Section Measurement</b>	<b>39</b>
55	2.1	Raw Cross Section . . . . .	39
56	2.1.1	Statistical Uncertainty . . . . .	40
57	2.1.2	Treatment of Systematics . . . . .	42
58	2.2	Corrections to the Raw Cross Section . . . . .	42
59	2.2.1	Treatment of Systematics . . . . .	42

# Acknowledgements

*“Dunque io ringrazio tutti quanti.  
Specie la mia mamma che mi ha fatto così funky.”*  
– Articolo 31, Tanqi Funky, 1996 –

*“At last, I thank everyone.  
Especially my mom who made me so funky.”*  
– Articolo 31, Tanqi Funky, 1996 –

A lot of people are awesome, especially you, since you probably agreed to read this when it was a draft.

# Chapter 0

## Total Hadronic Cross Section Measurement Methodology

This chapter describes the general procedure employed to measure a total hadronic differential cross section in LArIAT. Albeit with small differences, both the  $(\pi^-, \text{Ar})$  and  $(K^+, \text{Ar})$  total hadronic cross section measurements rely on the same procedure described in details in the following sections. We start by selecting the particle of interest using a combination of beamline detectors and TPC information (Section ??). We then perform a handshake between the beamline information and the TPC tracking to assure the selection of the right TPC track (Section 0.2). Finally, we apply the “thin slice” method and measure the “raw” hadronic cross section (Section 0.3). A series of corrections are then evaluated to obtain the “true” cross section (Section 0.3.3).

At the end of this chapter, we show a sanity check of the methodology against MC truth information (Section 0.4).



## 0.1 Event Selection

The measurement of the ( $\pi^-$ ,Ar) and ( $K^+$ ,Ar) total hadronic cross section in LArIAT starts by selecting the pool of pion or kaon candidates and measuring their momentum. This is done through the series of selections on beamline and TPC information described in the next sections. The summary of the event selection in data is reported in Table 1.

### 0.1.1 Selection of Beamline Events

As shown in equation 5, we leverage the beamline particle identification and momentum measurement before entering the TPC as in input to evaluate the kinetic energy for the hadrons used in the cross sections measurements. Thus, we select the LArIAT data to keep only events whose wire chamber and time of flight information is registered (line 2 in in Table 1). Additionally, we perform a check of the plausibility of the trajectory inside the beamline detectors: given the position of the hits in the four wire chambers, we make sure the particle's trajectory does not cross any impenetrable material such as the collimator and the magnets steel (line 3 in in Table 1).

	Run-II Negative Polarity	Run-II Positive Polarity
Events Reconstructed in Beamline	158396	260810
Events with Plausible Trajectory	147468	240954
Beamline $\pi^-/\mu^-/e^-$ Candidate	138481	N.A.
Beamline $K^+$ Candidate	N.A	2837
Events Surviving Pile Up Filter	108929	2389
Events with WC2TPC Match	41757	1081
Events Surviving Shower Filter	40841	N.A.
Available Events For Cross Section	40841	1081

Table 1: Number of data events for Run-II Negative and Positive polarity

### 99 0.1.2 Particle Identification in the Beamline

100 In data, the main tool to establish the identity of the hadron of interest is the LArIAT  
 101 tertiary beamline, in its function of mass spectrometer. We combine the measurement  
 102 of the time of flight,  $TOF$ , and the beamline momentum,  $p_{Beam}$ , to reconstruct the  
 103 invariant mass of the particles in the beamline,  $m_{Beam}$ , as follows

$$m_{Beam} = \frac{p_{Beam}}{c} \sqrt{\left(\frac{TOF * c}{l}\right)^2 - 1}, \quad (1)$$

104 where  $c$  is the speed of light and  $l$  is the length of the particle's trajectory between  
 105 the time of flight paddels.

106 Figure 1 shows the mass distribution for the Run II negative polarity runs on the  
 107 left and positive polarity runs on the right. We perform the classification of events  
 108 into the different samples as follows:

- 109 •  $\pi/\mu/e$ : mass < 350 MeV
- 110 • kaon: 350 MeV < mass < 650 MeV
- 111 • proton: 650 MeV < mass < 3000 MeV.

112 Lines 4 and 5 in in Table 1 show the number of negative  $\pi/\mu/e$  and positive  $K$   
 113 candidates which pass the mass selection for LArIAT Run-II data.

### 114 0.1.3 TPC Selection: Halo Mitigation

115 The secondary beam impinging on LArIAT secondary target produces a plethora of  
 116 particles which propagates downstream. The presence of upstream and downstream  
 117 collimators greatly abates the number of particles tracing down the LArIAT tertiary  
 118 beamline. However, it is possible that more than one particle sneaks into the LArTPC  
 119 during its readout time: the TPC readout is triggered by the particle firing the

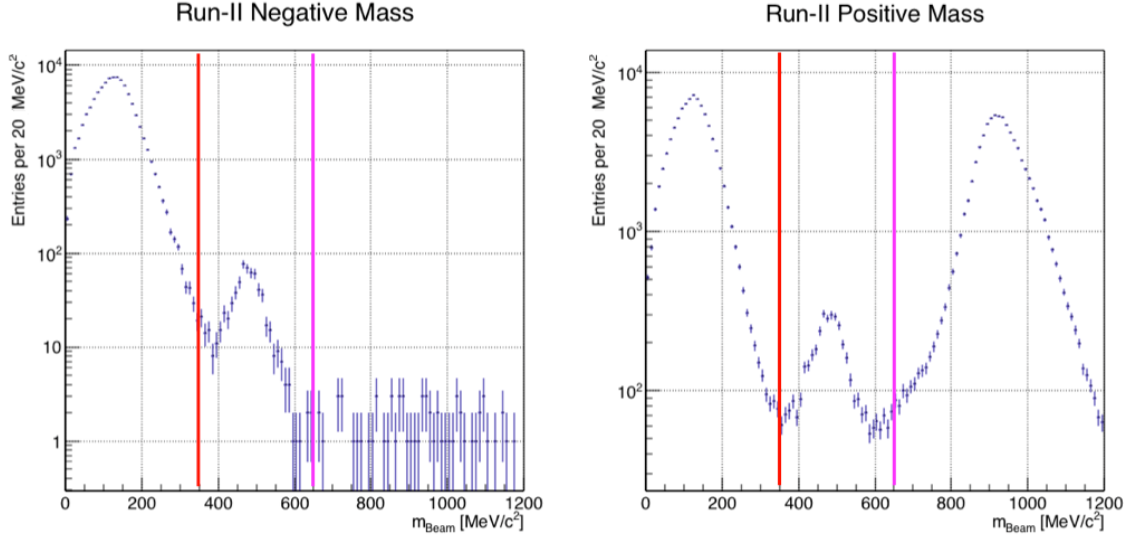


Figure 1: Distribution of the beamline mass as calculated according to equation 1 for the Run-II events reconstructed in the beamline, negative polarity runs on the left and positive polarity runs on the right. The classification of the events into  $\pi^\pm/\mu^\pm/e^\pm$ ,  $K^\pm$ , or (anti)proton is based on these distributions, whose selection cut are represented by the vertical colored lines.

beamline detectors, but particles from the beam halo might be present in the TPC at the same time. We call “pile up” the additional traces in the TPC. We adjusted the primary beam intensity between LArIAT Run I and Run II to reduce the presence of events with high pile up particles in the data sample. For the cross section analyses, we remove events with more than 4 tracks in the first 14 cm upstream portion of the TPC from the sample (line 6 in in Table 1).

#### 0.1.4 TPC Selection: Shower Removal

In the case of the  $(\pi^-, \text{Ar})$  cross section, the resolution of beamline mass spectrometer is not sufficient to select a beam of pure pions. In fact, muons and electrons survive the selection on the beamline mass. It is important to notice that the composition of the negative polarity beam is mostly pions, as will be discussed in section 1.2.1. Anyhow, we devise a selection on the TPC information to mitigate the presence of

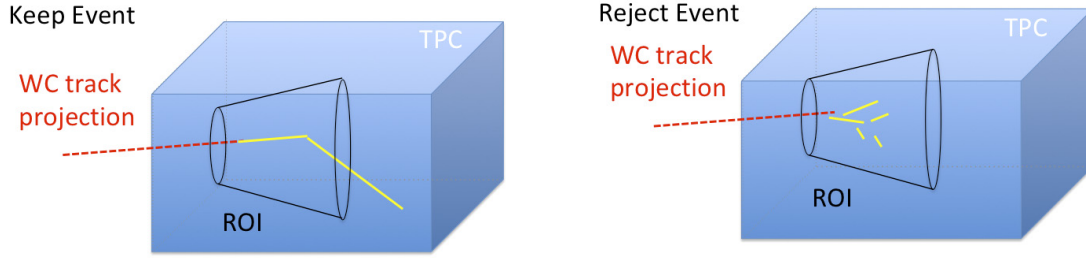


Figure 2: Visual rendering of the shower filter. The ROI is a cut cone, with a small radius of 4 cm, a big radius of 10 cm and an height of 42 cm (corresponding to 3 radiation lengths for electrons in Argon).

132 electrons in the sample used for the pion cross section. The selection relies on the  
 133 different topologies of a pion and an electron event in the argon: while the former  
 134 will trace a track inside the TPC active volume, the latter will tend to “shower”, i.e.  
 135 interact with the medium, producing bremsstrahlung photons which pair convert into  
 136 several short tracks. In order to remove the shower topology, we create a region of  
 137 interest (ROI) around the TPC track corresponding to the beamline particle (more  
 138 details on this in the next section). We look for short tracks contained in the ROI,  
 139 as depicted in figure 4: if more then 5 tracks shorter than 10 cm are in the ROI,  
 140 we reject the event. Line 8 in in Table 1) shows the number of events surviving this  
 141 selection.

## 142 **0.2 Beamline and TPC Handshake: the Wire Cham-** 143 **ber to TPC Match**

144 For each event passing the selection on its beamline information, we need to identify  
 145 the track inside the TPC corresponding to the particle which triggered the beamline  
 146 detectors, a procedure we refer to as “WC to TPC match” (WC2TPC for short).  
 147 In general, the TPC tracking algorithm will reconstruct more than one track in the  
 148 event, partially due to the fact that hadrons interact in the chamber and partially

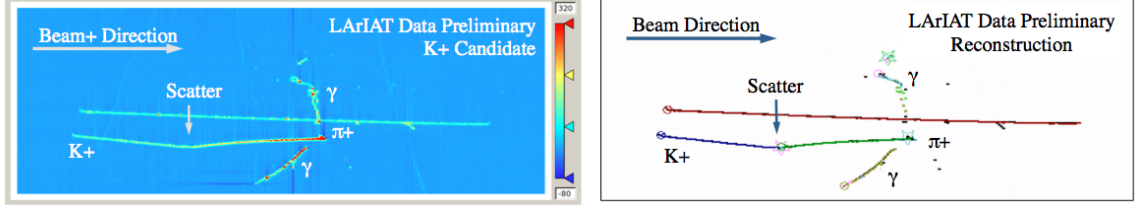


Figure 3: Kaon candidate event: on the right, event display showing raw quantities; on the left, event display showing reconstructed tracks. In the reconstructed event display, different colors represent different track objects. A kink is visible in the kaon ionization, signature of a hadronic interaction: the tracking correctly stops at the kink position and two tracks are formed. An additional pile-up track is so present in the event (top track).

149 because of pile up particles during the triggered TPC readout time, as shown in  
 150 figure 3.

151 We attempt to uniquely match one wire chamber track to one and only one re-  
 152 constructed TPC track. In order to determine if the presence of a match, we apply  
 153 a geometrical selection on the relative the position of the wire chamber and TPC  
 154 tracks. We start by considering only TPC tracks whose first point is in the first 2  
 155 cm upstream portion of the TPC for the match. We project the wire chamber track  
 156 to the TPC front face where we define the coordinates of the projected point as  $x_{FF}$   
 157 and  $y_{FF}$ . For each considered TPC track, we define  $\Delta X$  as the difference between  
 158 the  $x$  position of the most upstream point of the TPC track and  $x_{FF}$ .  $\Delta Y$  is defined  
 159 analogously. We define the radius difference,  $\Delta R$ , as  $\Delta R = \sqrt{\Delta X^2 + \Delta Y^2}$ . We de-  
 160 fine as  $\alpha$  the angle between the incident WC track and the TPC track in the plane  
 161 that contains them. If  $\Delta R < 4$  cm,  $\alpha < 8^\circ$ , a match between WC-track and TPC  
 162 reconstructed track is found. We describe how we determine the value for the radius  
 163 and angular selection in sec 1.3.1. In MC, we mimic the matching between the WC  
 164 and the TPC track by constructing a fake WC track using truth information at wire  
 165 chamber four. We then apply the same WC to TPC matching algorithm as in data.  
 166 We discard events with multiple WC2TPC matches. We use only those TPC tracks  
 167 that are matched to WC tracks in the cross section calculation.

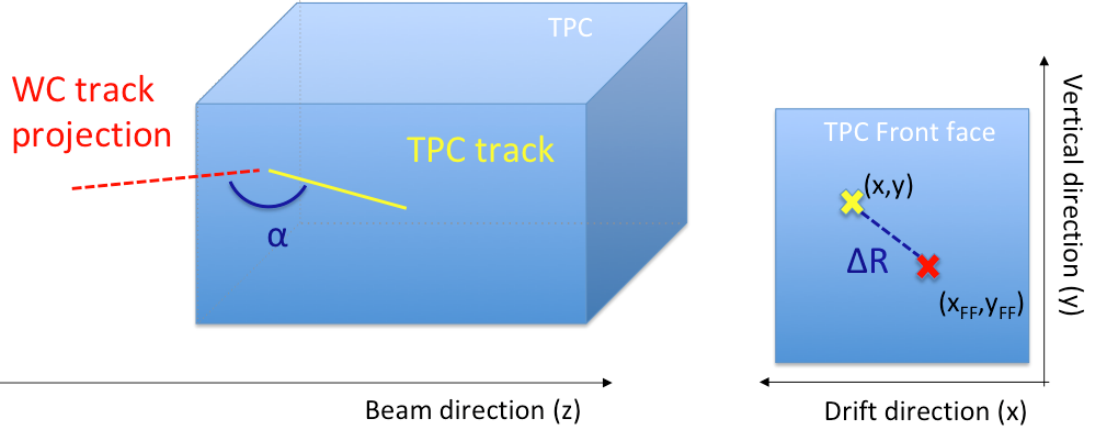


Figure 4: Visual rendering of the wire chamber to TPC match.

### 0.3 The Thin Slice Method

Once we have selected the pool of hadron candidates and we have identified the TPC track corresponding to the beamline event, we apply the thin slice method to measure the cross section, as the following sections describe.

#### 0.3.1 Cross Sections on Thin Target

Cross section measurements on a thin target have been the bread and butter of nuclear and particle experimentalists since the Geiger-Marsden experiments [65]. At their core, these types of experiments consist in shooting a beam of particles with a known flux on a thin target and recording the outgoing flux.

In general, the target is not a single particle, but rather a slab of material containing many diffusion centers. The so-called “thin target” approximation assumes that the target centers are uniformly distributed in the material and that the target is thin compared to the projectile interaction length,  $WC2TPC$  so that no center of interaction sits in front of another. In this approximation, the ratio between the number of particles interacting in the target  $N_{Interacting}$  and number of incident particles  $N_{Incident}$  determines the interaction probability  $P_{Interacting}$ , which is the complementary to one

184 of the survival probability  $P_{Survival}$ . Equation 2

$$P_{Survival} = 1 - P_{Interacting} = 1 - \frac{N_{Interacting}}{N_{Incident}} = e^{-\sigma_{TOT}n\delta X} \quad (2)$$

185 describes the probability for a particle to survive the thin target. This formula relates  
 186 the total cross section  $\sigma_{TOT}$ , the density of the target centers  $n$  and the thickness of  
 187 the target along the incident hadron direction  $\delta X$ , to the interaction probability<sup>1</sup>. If  
 188 the target is thin compared to the interaction length of the process considered, we can  
 189 Taylor expand the exponential function in equation 2 and find a simple proportionality  
 190 relationship between the number of incident and interacting particles, and the cross  
 191 section, as shown in equation 3:

$$1 - \frac{N_{Interacting}}{N_{Incident}} = 1 - \sigma_{TOT}n\delta X + O(\delta X^2). \quad (3)$$

192 Solving for the cross section, we find:

$$\sigma_{TOT} = \frac{1}{n\delta X} \frac{N_{Interacting}}{N_{Incident}}. \quad (4)$$

### 193 **0.3.2 Not-so-Thin Target: Slicing the Argon**

194 The interaction length of pions and kaons in argon is expected to be of the order  
 195 of 50 cm for pions and 100 cm for kaons. Thus, the LArIAT TPC, with its 90 cm  
 196 of length, is not a thin target. However, the fine-grained tracking of the LArIAT  
 197 LArTPC allows us to treat the argon volume as a sequence of many adjacent thin  
 198 targets.

199 As described in Chapter ??, LArIAT wire planes consist of 240 wires each. The  
 200 wires are oriented at +/- 60° from the vertical direction at 4 mm spacing, while the

---

1. The scattering center density in the target,  $n$ , relates to the argon density  $\rho$ , the Avogadro number  $N_A$  and the argon molar mass  $m_A$  as  $n = \frac{\rho N_A}{m_A}$ .

beam direction is oriented 3 degrees off the  $z$  axis in the  $XZ$  plane. The wires collect signals proportional to the energy loss of the hadron along its path in a  $\delta X = 4$  mm/ $\sin(60^\circ) \approx 4.7$  mm slab of liquid argon. Thus, one can think to slice the TPC into many thin targets of  $\delta X = 4.7$  mm thickness along the direction of the incident particle, making a measurement at each wire along the path.

Considering each slice  $j$  a “thin target”, we can apply the cross section calculation from Equation 2.1 iteratively, evaluating the kinetic energy of the hadron as it enters each slice,  $E_j^{kin}$ . For each WC2TPC matched particle, the energy of the hadron entering the TPC is known thanks to the momentum and mass determination by the tertiary beamline,

$$E_{FrontFace}^{kin} = \sqrt{p_{Beam}^2 - m_{Beam}^2} - m_{Beam} - E_{loss}, \quad (5)$$

where  $E_{loss}$  is a correction for the energy loss in the dead material between the beamline and the TPC front face. The energy of the hadron at each slab is determined by subtracting the energy released by the particle in the previous slabs. For example, at the  $j^{th}$  point of a track, the kinetic energy will be

$$E_j^{kin} = E_{FrontFace}^{kin} - \sum_{i < j} \Delta E_i, \quad (6)$$

where  $\Delta E_i$  is the energy deposited at each argon slice before the  $j^{th}$  point as measured by the calorimetry associated with the tracking.

If the particle enters a slice, it contributes to  $N_{Incident}(E^{kin})$  in the energy bin corresponding to its kinetic energy in that slice. If it interacts in the slice, it then also contributes to  $N_{Interacting}(E^{kin})$  in the appropriate energy bin. The cross section as a function of kinetic energy,  $\sigma_{TOT}(E^{kin})$  will then be proportional to the ratio

$$\frac{N_{Interacting}(E^{kin})}{N_{Incident}(E^{kin})}.$$



### 0.3.3 Corrections to the Raw Cross Section

Equation 2.1 is a prescription for measuring the cross section in case of a pure beam of the hadron of interest and 100% efficiency in the determination of the interaction point. For example, if LArIAT had a beam of pure pions and were 100% efficient in determining the interaction point within the TPC, the pion cross section in each energy bin would be given by

$$\sigma^{\pi^-}(E_i) = \frac{1}{n\delta X} \frac{N_{\text{Interacting}}^{\pi^-}(E_i)}{N_{\text{Incident}}^{\pi^-}(E_i)}. \quad (7)$$

Unfortunately, this is not the case. In fact, the selection used to isolate pions in the LArIAT beam allows for the presence of some muons and electrons as background. Also, the LArIAT TPC is not 100% efficient in determining the interaction point. Therefore we need to apply two corrections evaluated on the MC in order to extract the cross section from LArIAT data: the background subtraction and the efficiency correction. Still using the pion case as example, we estimate the pion cross section in each energy bin changing Equation 7 into

$$\sigma^{\pi^-}(E_i) = \frac{1}{n\delta X} \frac{N_{\text{Interacting}}^{\pi^-}(E_i)}{N_{\text{Incident}}^{\pi^-}(E_i)} = \frac{1}{n\delta X} \frac{\epsilon_i^{\text{inc}}[N_{\text{Interacting}}^{\text{TOT}}(E_i) - B_{\text{Interacting}}(E_i)]}{\epsilon_i^{\text{int}}[N_{\text{Incident}}^{\text{TOT}}(E_i) - B_{\text{Incident}}(E_i)]}, \quad (8)$$

where  $N_{\text{Interacting}}^{\text{TOT}}(E_i)$  and  $N_{\text{Incident}}^{\text{TOT}}(E_i)$  is the measured content of the interacting and incident histograms for events that pass the event selection,  $B_{\text{interacting}}(E_i)$  and  $B_{\text{Incident}}(E_i)$  represent the contributions from beamline background, and  $\epsilon_i^{\text{int}}$  and  $\epsilon_i^{\text{inc}}$  are the efficiency corrections for said histograms.

As we will show in section ??, the background subtraction for the interacting and incident histograms can be translated into a corresponding corrections  $C_{\text{Interacting}}^{\pi MC}(E_i)$  and  $C_{\text{Incident}}^{\pi MC}(E_i)$  and the cross section re-written as follows

$$\sigma^{\pi^-}(E_i) = \frac{1}{n\delta X} \frac{\epsilon_i^{inc} N_{Interacting}^{TOT}(E_i) C_{Interacting}^{\pi MC}(E_i)}{\epsilon_i^{int} N_{Incident}^{TOT}(E_i) C_{Incident}^{\pi MC}(E_i)}. \quad (9)$$

## 0.4 Procedure testing with truth quantities

The  $(\pi^-, \text{Ar})$  and  $(K^+, \text{Ar})$  total hadronic cross section implemented in Geant4 can be used as a tool to validate the measurement methodology. We describe here a closure test done on Monte Carlo to prove that the methodology of slicing the TPC retrieves the underlying cross section distribution implemented in Geant4 within the statistical uncertainty.

For pions in the considered energy range, the Geant4 inelastic model adopted to is “BertiniCascade”, while the elastic model “hElasticLHEP”. For kaons, the Geant4 inelastic model adopted to is “BertiniCascade”, while the elastic model “hElasticLHEP”.

For the validation test, we fire about a sample of pions and a sample of kaons inside the LArIAT TPC active volume using the Data Driven Monte Carlo (see section 1.2.2). We apply the thin-sliced method using only true quantities to calculate the hadron kinetic energy at each slab in order to decouple reconstruction effects from issues with the methodology. For each slab of 4.7 mm length along the path of the hadron, we integrate the true energy deposition as given by the Geant4 transportation model. Then, we recursively subtracted it from the hadron kinetic energy at the TPC front face to evaluate the kinetic energy at each slab until the true interaction point is reached. Since the MC is a pure beam of the hadron of interest and truth information is used to retrieve the interaction point, no correction is applied. Doing so, we obtain the true interacting and incident distributions for the considered hadron and we obtain the true MC cross section as a function of the hadron true kinetic energy.

Figure 5 shows the total hadronic cross section for argon implemented in Geant4

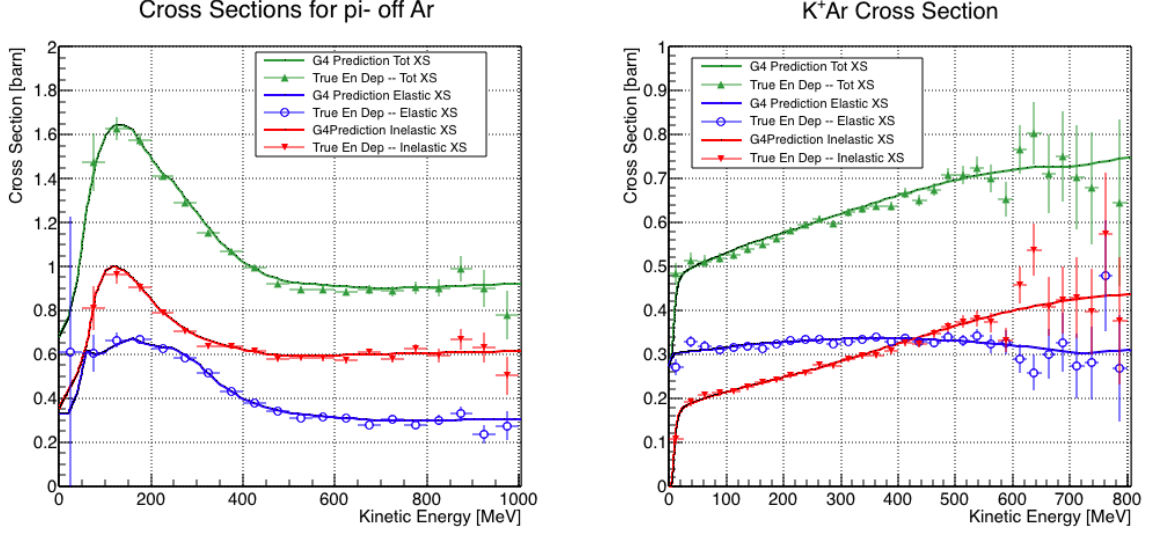


Figure 5: Hadronic cross sections for  $(\pi^-, \text{Ar})$  on the left and  $(K^+, \text{Ar})$  on the right as implemented in Geant4 10.01.p3 (solid lines) overlaid the true MC cross section as obtained with the sliced TPC method (markers). The total cross section is shown in green, the elastic cross section in blue and the inelastic cross section in red.

10.01.p3 (solid lines) overlaid with the true MC cross section as obtained with the  
sliced TPC method (markers) for pions on the left and kaons on the right; the total  
cross section is shown in green, the elastic cross section in blue and the inelastic  
cross section in red. The nice agreement with the Geant4 distribution and the cross  
section obtained with the sliced TPC method gives us confidence in the validity of  
the methodology.

# Chapter 1

## Preparatory Work

This chapter describes the preparatory work done on the the data and Monte Carlo samples used for the cross section analyses. This entails the choice of the data set and the production of the information needed to construct the Monte Carlo Simulation (section 1.1), the construction and use of said Monte Carlo simulation (section 1.2), the study and optimization of the tracking in the TPC for the cross section analyses (section 1.3), the calibration of the calorimetry response and related energy studies (section 1.4).

### 1.1 Cross Section Analyses Data Set

We choose LArIAT Run-II as the data period for the  $(\pi^-, \text{Ar})$  and  $(K^+, \text{Ar})$  total hadronic cross section analyses. Data taking for the this period started on 03/15/2016 and ended on 07/31/2016. Since we are interested in beamline and TPC information, we ask basic requirements on the operational status of the time of fight, wire chambers and TPC to form the good run list for this period, which we informally call “lovely runs”.

The subset of lovely runs chosen for the  $(\pi^-, \text{Ar})$  total hadronic cross section analysis includes only the -60A and -100A magnet configurations in negative polarity,

even if LArIAT explored several other beamline configurations during Run-II. The -60A and -100A combined data set accounts for approximately 90% of the total Run-II negative polarity runs. Since the production of beamline Monte Carlo depends on the wanted beamline configuration, the choice of only two beamline settings limits the need for beamline MC production.

Similarly, the subset of lovely runs chosen for the  $(K^+, \text{Ar})$  total hadronic cross section analysis includes only the +60A and +100A magnet configurations in positive polarity. It should be noted that kaons are extremely rare in the +60A sample, thus the data sample for the  $(K^+, \text{Ar})$  cross section after the mass selection is about 90% +100A runs, as shown in Table 1.1.

For the first measurements in LArIAT that uses both beamline and TPC information, we choose strict requirements on the reconstruction of the WC tracks, the so-called “Picky Track” sample (see ??). This choice presents two advantages: the uncertainty on the momentum reconstruction for the “Picky Tracks” sample is smaller compared to the “High Yield” sample, and the comparison with the beamline MC results is straightforward. A possible future update and cross check of these analysis would be the use of the High Yield sample, where the statistics is about three times higher.

The breakdown of beamline events as a function of the magnets settings is shown in Table 1.1. The choice of the data sets determines the production of beamline MC and serves as basis for the production of Data Driven MC, as shown in the next sections.

	I = 60 A	I = 100 A	Total
Data Events after $\pi/\mu/e$ Mass Selection	67068	71413	138481
Data Events after $K$ Mass Selection	274	2563	2837

Table 1.1: Number of data events which fit the  $\pi/\mu/e$  or  $K$  mass hypothesis as a function of magnet settings.

## 311 1.2 Construction of a Monte Carlo Simulation for 312 LArIAT

313 For the simulation of LArIAT events and their particle make up, we use a combination  
314 of two MC generators: the G4Beamline Monte Carlo and the Data Driven single  
315 particle Monte Carlo (DDMC). We use the G4Beamline MC to simulate the particle  
316 transportation in the beamline and calculate the particle composition of the beam just  
317 after the fourth Wire Chamber (WC4). In order to simulate the beamline particles  
318 after WC4 and in the TPC, we use the DDMC.

### 319 1.2.1 G4Beamline

320 G4Beamline simulates the beam collision with the LArIAT secondary target, the  
321 energy deposited by the particles in the LArIAT beamline detectors, and the action  
322 of the LArIAT magnets, effectively accounting for particle transportation through the  
323 beam line from the LArIAT target until “Big Disk”, a fictional, void detector located  
324 just before the LArIAT cryostat. At the moment of this writing, G4Beamline does  
325 not simulated the responses of the beam line detectors. It is possible to interrogate  
326 the truth level information of the simulated particles in several points of the geometry.  
327 In order to ease the handshake between G4Beamline and the DDMC, we ask for the  
328 beam composition just after WC4. Since LArIAT data are taken under different  
329 beam conditions, we need to simulate separately the beam composition according to  
330 the magnets’ settings and the secondary beam intensity with G4Beamline. For the  
331 pion cross section analysis the relevant beam conditions are secondary beam energy  
332 of 64 GeV, negative polarity magnet with current of 100 A and 60 A. For the kaon  
333 cross section analysis the relevant beam conditions is a secondary beam energy of 64  
334 GeV, positive polarity magnet with current of 100 A.

	I = -60 A	I = -100 A
G4Pions	68.8 %	87.4 %
G4Muons	4.6 %	3.7 %
G4Electrons	26.6 %	8.9 %

Table 1.2: Simulated beamline composition per magnet settings

### 335 Beam Composition for Negative Pion Cross Section

336 Even if pions are by far the biggest beam component in negative polarity runs, the  
337 LArIAT tertiary beam is not a pure pion beam. While useful to discriminate between  
338 pions, kaons, and protons, the beamline detectors are not sensitive enough to discrim-  
339 inate among the lighter particles in the beam: electrons, muons and pions fall under  
340 the same mass hypothesis. Thus, we need to assess the contamination from beamline  
341 particles other than pions in the event selections used for the pion cross section analy-  
342 sis and correct for its effects. The first step of this process is assessing the percentage  
343 of electrons and muons in the  $\pi/\mu/e$  beamline candidates via the G4Beamline MC.  
344 The full treatment of the beamline contamination in the pion cross section calculation  
345 is described in section ???. Since the beamline composition is a function of the magnet  
346 settings, we simulate separately events for magnet current of -60A and -100A. Figure  
347 1.1 shows the momentum predictions from G4Beamline overlaid with data for the  
348 60A runs (left) and for the 100A runs (right). The predictions for electrons, muons  
349 and pions have been staggered and their sum is area normalized to data. Albeit not  
350 perfect, these plots show a reasonable agreement between the momentum shapes in  
351 data and MC. We attribute the difference in shape to the lack of simulation of the  
352 WC efficiency in the MC which is momentum dependent and leads to enhance the  
353 number events in the center of the momentum distribution.

354 Table 1.2 shows the beam composition per magnet setting after the mass selection  
355 according to the G4Beamline simulation.

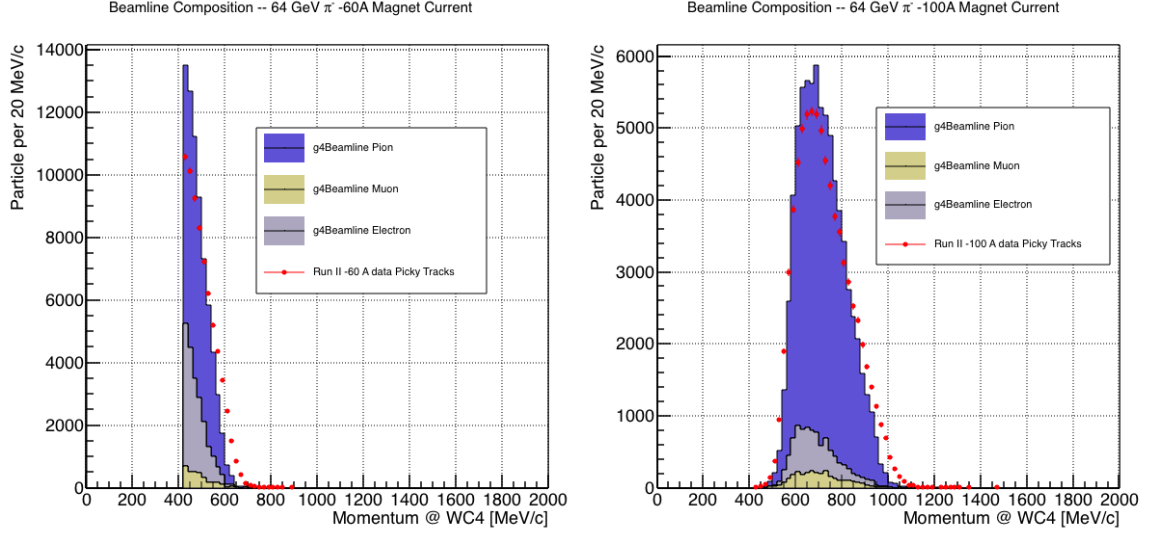


Figure 1.1: Beam composition for the -60A runs (left) and -100A runs (right). The solid blue plot represents the simulated pion content, the yellow plot represents the simulated muon content and the grey plot represents the simulated electron content. The plots are area normalized to the number of data events, shown in red.

### 356 Beam Composition for Positive Kaon Cross Section

357 In the positive polarity runs, the tertiary beam composition is mainly pions and pro-  
 358 tons. The left side of Figure 1.2 shows the predictions for the momentum spectra  
 359 for the 100A positive runs according to G4Beamline (solid colors) overlaid with data  
 360 (black points). Since the LArIAT beamline detectors can discriminate between kaons  
 361 and other particles, we do not rely on the G4Beamline simulation to estimate the  
 362 beamline contamination in the pool of kaon candidates (as in the case of the pion  
 363 cross section), but rather we use a data drive approach. The basic idea of this data  
 364 driven approach is to estimate the bleed over from high and low mass peaks under the  
 365 kaon peak by fitting the tails of the  $\pi/\mu/e$  and proton mass distributions, as shown  
 366 in Figure 1.2 right side. Since the shape of the tails is unknown, the estimate is done  
 367 multiple times varying the range and shape for reasonable functions. For example, to  
 368 estimate the proton content under the kaon peak, we start by fitting the left tail of  
 369 the proton mass distribution with a gaussian function between  $650 \text{ MeV}/c^2$  and  $750$



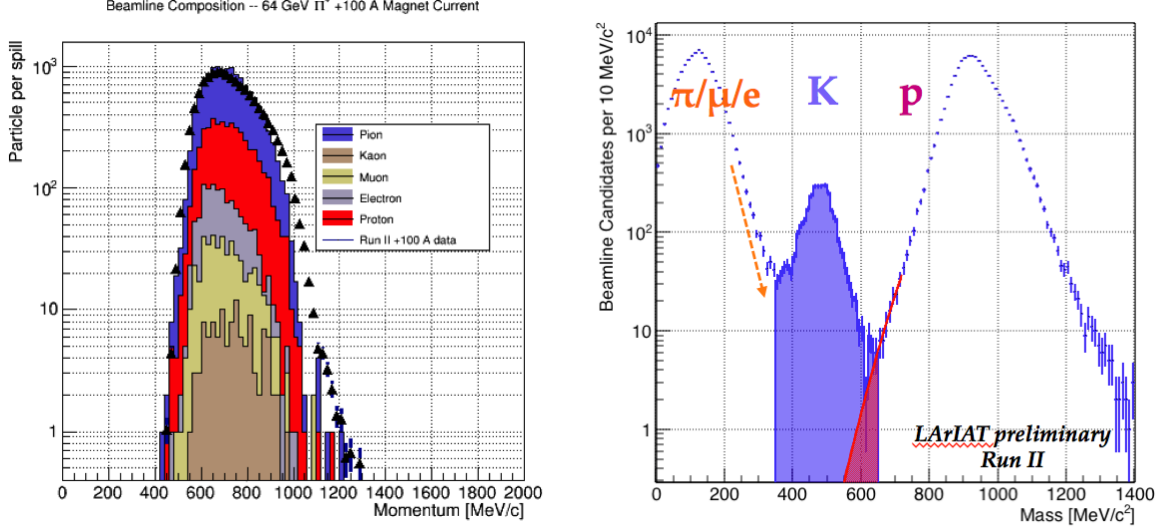


Figure 1.2: *Left*. Beam composition for the +100A runs after WC4 (no mass selection applied). The solid blue plot represents the simulated pion content, the yellow plot represents the simulated muon content and the grey plot represents the simulated positron content, the red the proton content and the mustard the kaon content. The plots are area normalized to the number of data events, shown in black. *Right*. Mass distribution for the Run-II positive runs, where the area under the kaon mass peak is highlighted in purple. The area under the extension of a possible fit for the proton tail is highlighted in red.

370  $MeV/c^2$ . We extend the fit function under the kaon peak and integrate the between  
371  $350-650 MeV/c^2$ . We integrate the mass histogram in the same range and calculate  
372 the proton contamination as the ratio between the two integrals. We repeat this pro-  
373 cedure for several fit shapes (gaussian, linear and exponential functions are used) and  
374 tail ranges. Finally, we calculate the contamination as the weighted average of single  
375 estimates, where the weights are calculated to be the  $1/\chi^2$  of the tail fits. The pro-  
376 cedure is repeated for lighter particles mass peak independently. With 12 iterations  
377 of this method we find a proton contamination of  $0.2 \pm 0.5 \%$  and a contamination  
378 from the lighter particles of  $5 \pm 2 \%$ .

### 1.2.2 Data Driven MC

The Data Driven single particle Monte Carlo (DDMC) is a single particle gun which simulates the particle transportation from WC4 into the TPC leveraging on the beam-line data information. The DDMC uses the data momentum and position at WC4 to derive the event generation: a general sketch of the DDMC workflow is shown in Figure 1.3.

When producing a DDMC sample, beam line data from a particular running period and/or running condition are selected first. For example, data for the negative 60A runs and for the negative 100A runs inform the event generation stage of two different DDMC samples. Figure 1.4 schematically shows the data quantities of interest leveraged from data: the momentum ( $P_x, P_y, P_z$ ) and position ( $X, Y$ ) at WC4. For each data event, we obtain the particle position ( $X, Y$ ) at WC4 directly from the data measurement; we calculate the components of the momentum using the beamline measurement of the momentum magnitude in conjunction with the hits on WC3 and WC4 to determine the direction of the momentum vector, as described in section ??.

The momentum and position of the selected data form a 5-dimensional tuple, which we sample thousands of times through a 5-dimensional hit-or-miss sampling procedure to generate the MC events. This produces MC  $P_x, P_y, P_z, X, Y$  distributions with the same momentum and position distributions as data, with the additional benefit of accounting for the correlations between the considered variables. As an example, the results of the DDMC generation compared to data for the kaon +100A sample are shown in figure ?? for the  $P_z, X$  and  $Y$  distributions; as expected, MC and data agree within the statistical uncertainty by construction. A LArSoft simulation module then launches single particle MC from  $z = -100$  cm (the location of the WC4) using the MC generated events. The particles are free to decay and interact in their path from WC4 to the TPC according to the Geant4 simulation.

Using the DDMC technique ensures that the MC and data particles have very

406 similar momentum, position and angular distributions at WC4 and allows us to use  
 407 the MC sample in several occasions, for example to calibrate the energy loss upstream  
 408 of the TPC (see Section 1.2.3) or to study the tracking and the calorimetric perfor-  
 409 mance (sections 1.3 and 1.4). A small caveat is in order here: the DDMC is a single  
 410 particle Monte Carlo, which means that the beam pile-up is not simulated.

411 Six samples are the basis for the MC used in the pion cross section measurement:  
 412 three samples of  $\sim 340000$  pions, muons and electrons to simulate the negative 60A  
 413 runs, and three samples of  $\sim 340000$  pions, muons and electrons for the negative 100A  
 414 runs.

415 The MC used for the kaon cross section analysis is a sample of **NUMBERS** kaons.

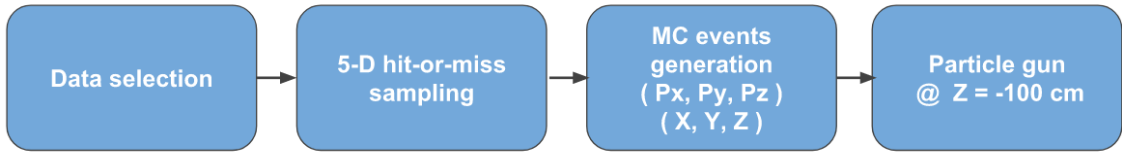


Figure 1.3: Workflow for Data Driven single particle Monte Carlo production.

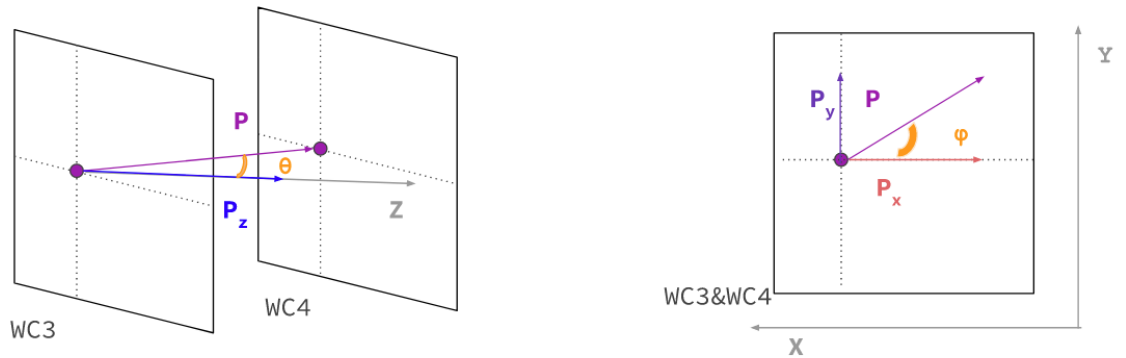


Figure 1.4: Scheme of the quantities of interest for the DDMC event generation:  $P_x, P_y, P_z, X, Y$  at WC4.

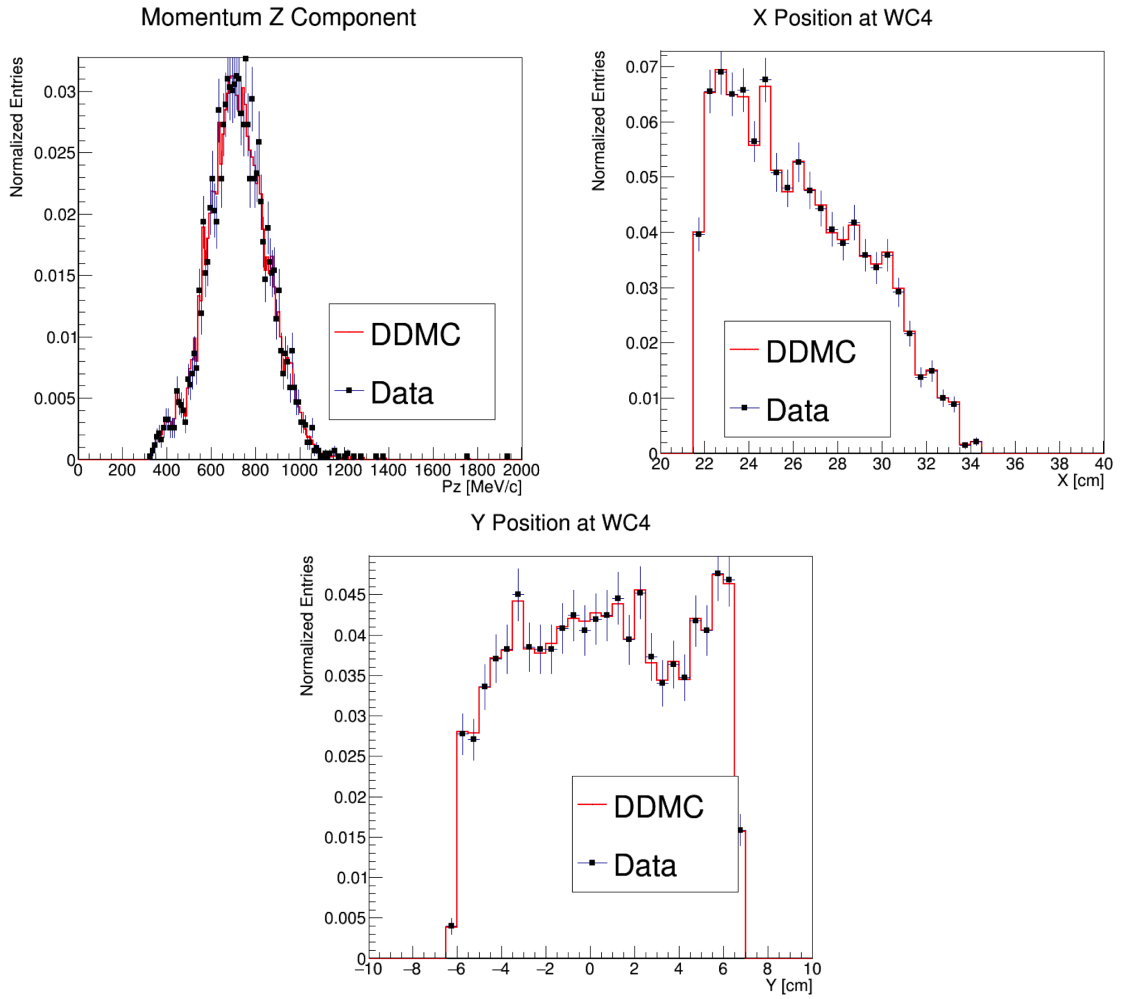


Figure 1.5: Comparison between generated quantities and data distributions for the 100A kaon sample: Z component of the momentum at WC4 (top left), X position at Wire Chamber 4 (top right), Y position at Wire Chamber 4 (bottom).

### 416 1.2.3 Estimate of Energy Loss before the TPC

417 The beamline particles travel a path from where their momentum is measured in  
 418 the beamline until they are tracked again inside the TPC. In the LArIAT geometry,  
 419 a particle leaving the WC4 will encounter the materials listed in Table 1.3 before  
 420 being registered again. The energy lost by the particle in this non-instrumented  
 421 material modifies the particle’s kinetic energy and directly affects the cross section  
 422 measurement, as shown in equation 5.

Material	density [g/cm <sup>3</sup> ]	width [cm]
Fiberglass laminate (G10)	1.7	1.28
Liquid Argon	1.4	3.20
Stainless Steel	7.7	0.23
Titanium	4.5	0.04
Air	$1.2 \cdot 10^{-3}$	89.43
Plastic Scintillator	1.03	1.20 (+ 1.30)

Table 1.3: LArIAT material budget from WC4 to the TPC Front Face.

We derive an estimate of the energy loss between the beamline momentum measurement and the TPC ( $E_{loss}$ ) from the pion DDMC sample, since this quantity is not measurable directly on data. The  $E_{loss}$  distribution for the 60A and 100A pion sample is shown in figure 1.6, left and right respectively. A clear double peaked structure is visible, which is due to the particles either missing or hitting the HALO paddle: a schematic rendering of this occurrence is shown in figure 1.7. The kinematic at WC4 determines the trajectory of a particle and whether or not it will hit the halo paddle. In figure 1.8 , we plot the true horizontal component of the momentum  $P_x$  versus the true  $X$  position at WC4 for pions missing the halo paddle (left) and for pions hitting the halo paddle (right) for the 60A MC simulation runs – analogous plots are obtained with the 100A simulation. These distributions can be separated drawing a line in this position-momentum space. We use a logistic regression [12] as a classifier to find the best separating line, shown in both plots as the red line. We classify as

“hitting the halo paddle” all pions whose  $P_x$  and  $X$  are such that

$$P_x + 0.02 * X - 0.4 < 0$$

and as “missing the halo paddle” all pions whose  $P_x$  and  $X$  are such that

$$P_x + 0.02 * X - 0.4 > 0,$$

where the coefficients of the line are empirically found by the logistic regression estimation. Overall, this simple methode classifies in the right category (hit or miss) about 86% of the pion events. In MC, we assign  $E_{loss} = 32 \pm 4$  MeV for pion events classified as “hitting the halo paddle”; we assign  $E_{loss} = 24 \pm 3$  MeV for pion events classified as “missing the halo paddle”. We apply the same classifier on data. A scan of the simulated geometry showed an excess of 3 cm of un-instrumented argon compared with the surveyed detector geometry. We account for this difference by assigning in data  $E_{loss} = 24 \pm 6$  MeV for pion events classified as “hitting the halo paddle” and  $E_{loss} = 17 \pm 6$  MeV for pion events classified as “missing the halo paddle”, where the uncertainty is derived as the standard deviation of the double peaked distribution.

The summary of the values for used for  $E_{Loss}$  for the pion sample is listed in table 1.4 with the analogous results for the study on the kaon case.

	$E_{loss}$ [MeV]	
	Hitting Halo	Missing Halo
Pion MC	$32 \pm 4$	$24 \pm 3$
Pion Data	$25 \pm 6$	$17 \pm 6$
Kaon MC	$37 \pm 5$	$31 \pm 4$
Kaon Data	$26 \pm 6$	$22 \pm 6$

Table 1.4: Energy loss for pions and kaons.

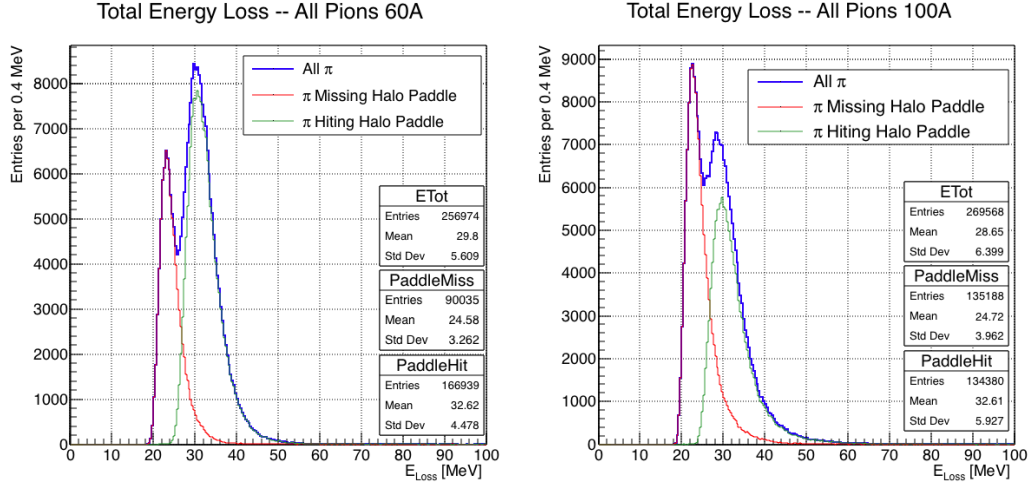


Figure 1.6: True energy loss between WC4 and the TPC front face according to the MC simulation of negative pions of the 60A runs (left) and of the 100A runs (right). The distribution for the whole data sample is shown in blue, the distribution for the pions missing the halo is shown in red, and the distribution for the pions hitting the halo is shown in green.

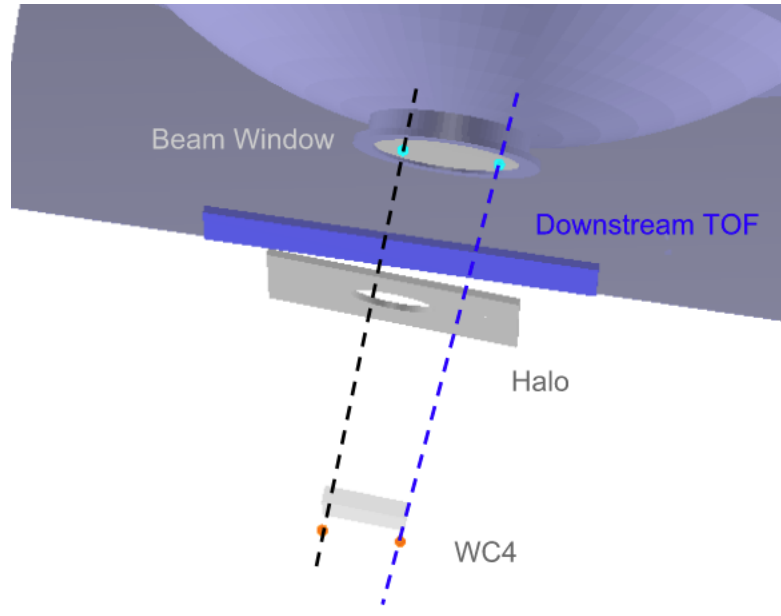


Figure 1.7: Schematic rendering of the particle path between WC4 and the TPC front face. The paddle with the hollow central circle represents the Halo paddle. We illustrate two possible trajectories: in black, a trajectory that miss the paddle and goes through the hole in the Halo, in blue a trajectory that hits the Halo paddle and goes through the scintillation material.

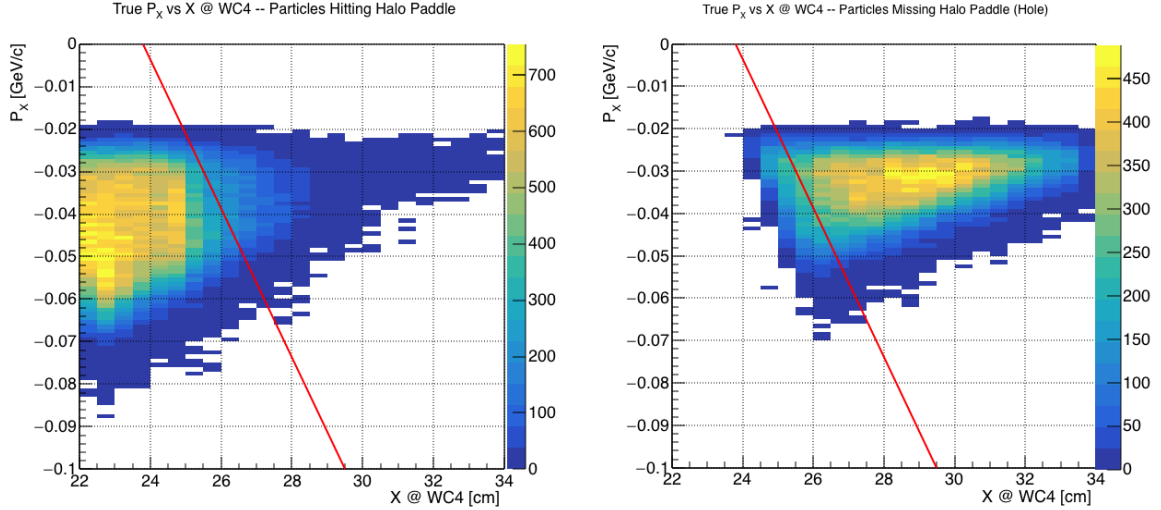


Figure 1.8: Horizontal component of the true momentum vs the horizontal position at WC4 for MC simulated pions of the 60A runs. The plot on the left shows the distribution for pion that miss the halo paddle and the plot on the right shows the distributions for pions that hit the halo. The form of the classifier is overlaid to both plots (red line).

### 1.3 Tracking Studies

In this section, we describe three studies. The first is a justification of the selection criteria for the beamline handshake with the TPC information. We perform this study to boost the correct identification of the particles in the TPC associated with the beamline information, while maintaining sufficient statistics for the cross section measurement. The second study is an optimization of the tracking algorithm, with the scope of maximizing the identification of the hadronic interaction point inside the TPC. These two studies are related, since the optimization of the tracking is performed on TPC tracks which have been matched to the wire chamber track; in turn, the tracking algorithm for TPC tracks determines the number of reconstructed tracks in each event used to try the matching with the wire chamber track. Starting with a sensible tracking reconstruction, we perform the WC2TPC matching optimization first, then the tracking optimization. The WC2TPC match purity and efficiency are then calculated again with the optimized tracking.



450 The third study is an evaluation of the angular resolution of the tracking algorithm  
451 in data and MC, which is particularly important in the context of the cross section  
452 analyses.

### 453 **1.3.1 Study of WC to TPC Match**

454 Plots I want in this section:

- 455 1. WC2TPC MC DeltaX, DeltaY and  $\alpha$

456 Scope of this study is assessing the goodness of the wire chamber to TPC match  
457 on Monte Carlo and decide the selection values we will use on data. A word of caution  
458 is necessary here. With this study, we want to minimize pathologies associated with  
459 the presence of the primary hadron itself, e.g. the incorrect association between the  
460 beamline hadron and its decay products inside the TPC. Assessing the contamination  
461 from pile-up<sup>1</sup>, albeit related, is beyond the scope of this study.

462 In MC, we are able to define a correct WC2TPC match using the Geant4 truth  
463 information. We are thus able to count how many times the WC tracks is associated  
464 with the wrong TPC reconstructed track.

465 We define a correct match if the all following conditions are met:

- 466 - the length of the true primary Geant4 track in the TPC is greater than 2 cm,
- 467 - the length of the reconstructed track length is greater than 2 cm,
- 468 - the Z position of the first reconstructed point is within 2 cm from the TPC  
469 front face
- 470 - the distance between the reconstructed track and the true entering point is the  
471 minimum compared with all the other reconstructed tracks.

---

1. We remind the reader that the DDMC is a single particle Monte Carlo, where the beam pile up is not simulated.

472 In order to count the wrong matches, we consider all the reconstructed tracks  
 473 whose Z position of the first reconstructed point lies within 2 cm from the TPC front  
 474 face. Events with true length in TPC  $< 2$  cm are included. Since hadrons are shot  
 475 100 cm upstream from the TPC front face, the following two scenarios are possible  
 476 from a truth standpoint:

477  $[Ta]$  the primary hadron decays or interact strongly before getting to the TPC,  
 478  $[Tb]$  the primary hadron enters the TPC.

479 As described in Section 0.2, we define a WC2TPC match according to the relative  
 480 position of the WC and TPC track parametrized with  $\Delta R$  and the angle between  
 481 them, parametrized with  $\alpha$ . Once we choose the selection values  $r_T$  and  $\alpha_T$  to de-  
 482 termine a reconstructed WC2TPC match, the following five scenarios are possible in  
 483 the truth to reconstruction interplay :

- 484 1) only the correct track is matched
- 485 2) only one wrong track is matched
- 486 3) the correct track and one (or more) wrong tracks are matched
- 487 4) multiple wrong tracks matched.
- 488 5) no reconstructed tracks are matched

489 Since we keep only events with one and only one match, we discard cases 3), 4)  
 490 and 5) from the events used in the cross section measurement. For each set of  $r_T$  and  
 491  $\alpha_T$  selection value, we define purity and efficiency of the selection as follows:

$$\text{Efficiency} = \frac{\text{Number of events correctly matched}}{\text{Number of events with primary in TPC}}, \quad (1.1)$$

$$\text{Purity} = \frac{\text{Number of events correctly matched}}{\text{Total number of matched events}}. \quad (1.2)$$

Figure 1.9 shows the efficiency (left) and purity (right) for WC2TPC match as a function of the radius,  $r_T$ , and angle,  $\alpha_T$ , selection value. It is apparent how both efficiency and purity are fairly flat as a function of the radius selection value at a given angle. This is not surprising. Since we are studying a single particle gun Monte Carlo sample, the wrong matches can occur only for mis-tracking of the primary or for association with decay products; decay products will tend to be produced at large angles compared to the primary, but could be fairly close to the in  $x$  and  $y$  projection of the primary. The radius cut would play a key role in removing pile up events.

For LArIAT cross section measurements, we generally prefer purity over efficiency, since a sample of particles of a pure species will lead to a better measurement. Obviously, purity should be balanced with a sensible efficiency to avoid rejecting the whole sample.

We choose  $(\alpha_T, r_T) = (8 \text{ deg}, 4 \text{ cm})$  and get a MC 85% efficiency and 98% purity for the kaon sample and a MC 95% efficiency and 90% purity for the pion sample.

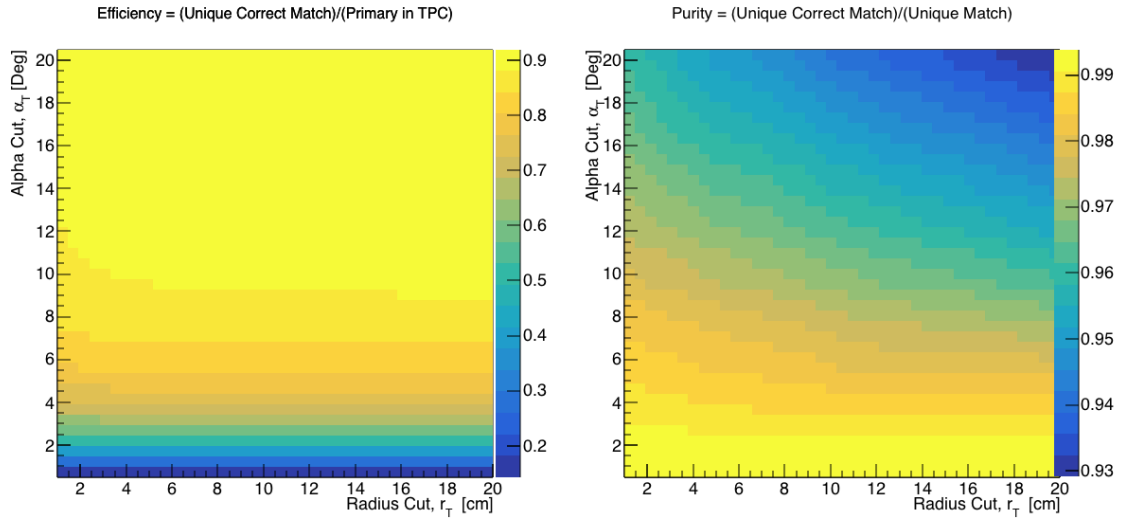


Figure 1.9: Efficiency (left) and purity (right) for WC2TPC match as a function of the radius and angle selections for the kaon sample.

## 506 1.3.2 Tracking Optimization

### 507 1.3.3 Angular Resolution

508 Scope of this study is to understand and compare the tracking performances and  
509 angular resolution of the TPC tracking on data and MC. We use the angular resolution  
510 of the tracking to determine the value of smallest angle that we can reconstruct with  
511 a non-zero efficiency, effectively determining a selection on the angular distribution  
512 of the cross section measurement due to the tracking performance. This study is  
513 performed on the pion sample, but its results are extrapolated to the kaon case.

514 We start by selecting all the WC2TPC matched tracks used for the cross section  
515 analysis. These tracks can contain from a minimum of 3 3D-space points to a maxi-  
516 mum of 240 3D-space points. We fit a line to all the 3D-space points associated with  
517 the track. For each track we calculate the average distance between each point in  
518 space and the fit line as follows

$$\bar{d} = \frac{\sum_i^N d_i}{N}, \quad (1.3)$$

519 where  $N$  is the number of 3D-space points of the track and  $d_i$  is the distance of the  
520  $i$ -th space point to the line fit. Several tests to compare the goodness of fit between  
521 data and MC have been considered. We decided to use  $\bar{d}$  for its straightforward  
522 interpretation. The  $\bar{d}$  distribution for data and MC is shown in Figure 1.10 and  
523 shows a relatively good agreement between data and MC.

524 A visual representation of the procedure used to evaluate the angular resolution is  
525 shown in Figure 1.12. For each track, we order the space points according to their Z  
526 position along the positive beam direction (panel a) and we split them in two sets: the  
527 first set contains all the points belonging to the first half of the track and the second  
528 set contains all the points belonging the second half of the track. We remove the last  
529 four points in the first set and the first four points in the second set, so to have a  
530 gap in the middle of the original track (panel b). We fit the first and the second set

531 of points with two lines (panel c). We then calculate the angle between the fit of the  
 532 first and second half  $\alpha$  (panel d). The angle  $\alpha$  determines the spatial resolution of  
 533 the tracking. The distributions for data and MC for  $\alpha$  are given in Figure 1.11. The  
 534 mean of the data and MC angular resolution are respectively

$$\bar{\alpha}_{Data} = (5.0 \pm 4.5) \text{ deg}, \quad (1.4)$$

$$\bar{\alpha}_{MC} = (4.5 \pm 3.9) \text{ deg}. \quad (1.5)$$

535 Interaction angles smaller than the angle resolution are indistinguishable for the  
 536 reconstruction. Therefore, we assess our ability to measure the cross section to be  
 537 limited to interaction angles greater than 5.0 deg. More accurate studies of the angular  
 538 resolution as a function of the kinetic energy and track length, albeit interesting, are  
 539 left for an improvement of the analysis.

540 It is beneficial to take a moment to describe the definition of interaction angle.  
 541 In case of elastic scattering, the definition is straightforward: the interaction angle is  
 542 the angle between the incoming and outgoing pion, i.e.

$$\theta = \cos^{-1} \left( \frac{\vec{p}_{\text{incoming}} \cdot \vec{p}_{\text{outgoing}}}{|\vec{p}_{\text{incoming}}| |\vec{p}_{\text{outgoing}}|} \right). \quad (1.6)$$

543 In case of inelastic scattering, the presence of several topologies requires a more  
 544 complex definition, as shown in figure 1.13. We define the scattering angle as the  
 545 biggest of the angles between the incoming pion and the visible daughters, where the  
 546 visible daughters are charged particles that travel more than 0.47 cm in the detector  
 547 (see panel a); in case all the daughters are invisible, the angle is assigned to be 90  
 548 deg (see panel b). We chose this working definition of scattering angle for inelastic  
 549 scattering keeping in mind how our tracking reconstruction works: the tracking will  
 550 stop correctly in case of all the daughters are not visible in the detector and it is

likely to stop correctly if multiple daughters form an interaction vertex. The only “dangerous” case is the production of one charged daughter plus neutrals, which we can study with this working definition of scattering angle (see panel c).

We can see the effects of the angular resolution on the cross section by plotting the true Geant4 cross section for interaction angles greater than a minimum interaction angle. Figure 1.14 shows the true Geant4 cross section for interaction angles greater than 0 deg (green), 4.5 deg (red), 5.0 deg (blue) and 9.0 deg (yellow). A small 0.5 deg systematic shift between the mean of the data and MC angular resolution is present.

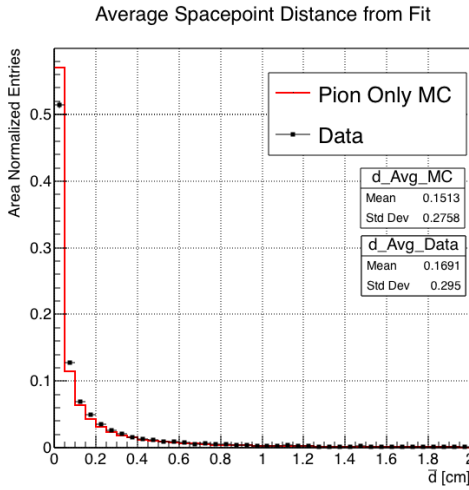


Figure 1.10: Distributions of the average distance between each 3D point in space and the fit line,  $\bar{d}$  for the data used in the pion cross section analysis and the pion only DDMC. The distributions are area normalized.

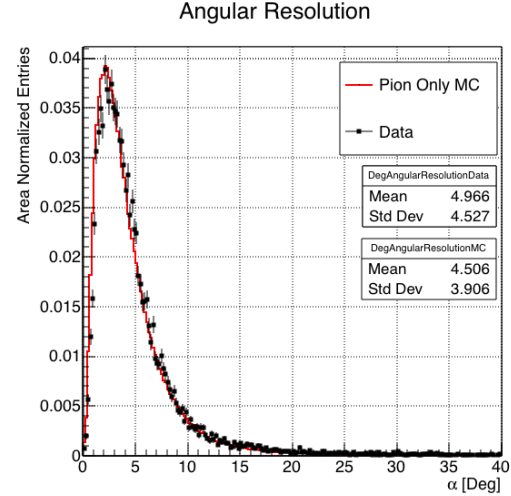


Figure 1.11: Distributions of angular resolution  $\alpha$  for data used in the pion cross section analysis and pion only DDMC. The distributions are area normalized.

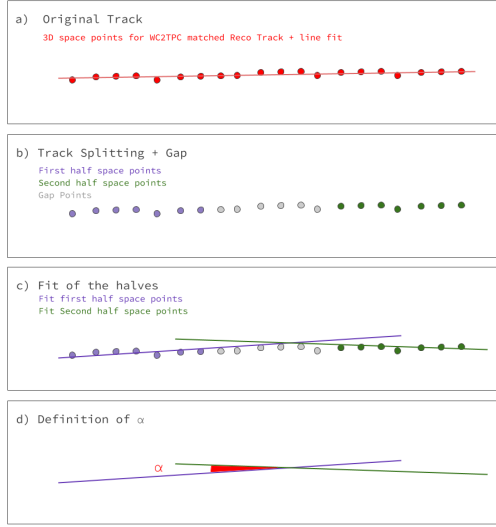


Figure 1.12: A visual representation of the procedure used to evaluate the angular resolution.

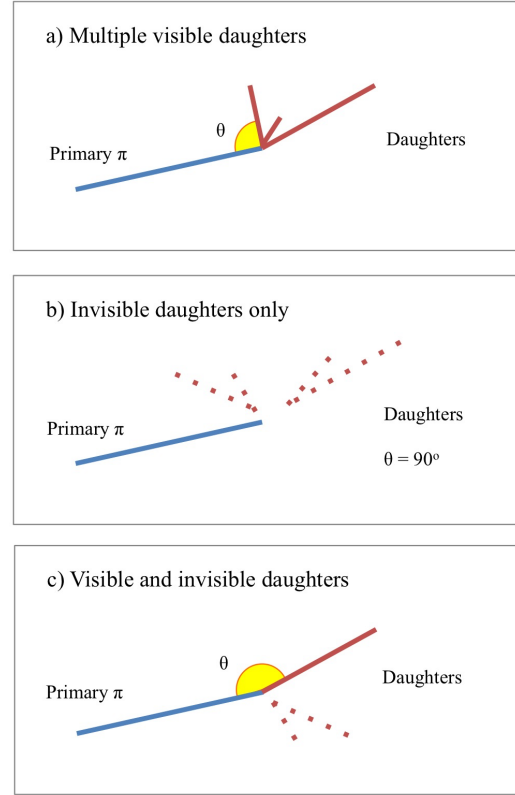


Figure 1.13: A visual representation of the scattering angle definition in case of inelastic scattering.

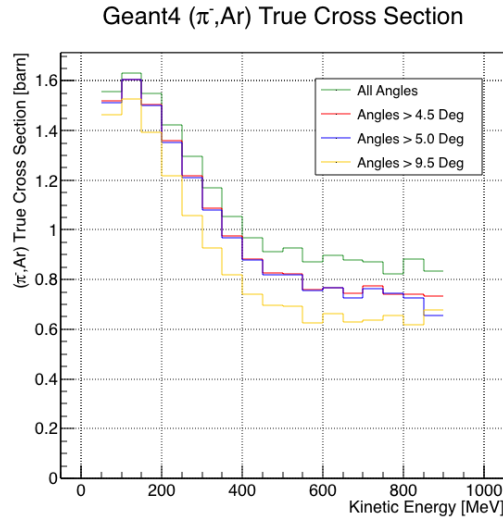


Figure 1.14: True ( $\pi^-$ , Ar) cross section for interaction angles greater than 0 deg (green), 4.5 deg (red), 5.0 deg (blue) and 9.0 deg (yellow).

## 559 1.4 Energy Calibration and Studies

### 560 1.4.1 Energy Calibration

### 561 1.4.2 Uncertainty on Kinetic Energy

562 The measured kinetic energy of a hadron candidate at each argon slab determines  
563 which bins of the interacting and incident histograms a selected event is going to fill.  
564 With this study, we determine the uncertainty of the kinetic energy measurement  
565 which we will propagate into the cross section measurement, as discussed in Section  
566 2.1.2 for the pion cross section and in Section ?? for the kaon cross section.

567 The kinetic energy of a hadron at the  $j^{\text{th}}$  slice of argon in the TPC is given by

$$KE_j = \sqrt{p_{Beam}^2 + m_{Beam}^2} - m_{Beam} - E_{Loss} - E_{FF-j}, \quad (1.7)$$

568 where  $p_{Beam}$  is the momentum measured by the beamline detectors,  $m_{Beam}$  is the  
569 mass of the hadron as reported in the PDG,  $E_{Loss}$  is the energy loss between the  
570 beamline and the TPC, and  $E_{FF-j}$  is the energy that the hadron deposited from the  
571 TPC front face until the  $j^{\text{th}}$  slice. The uncertainty on  $KE_j$  is then given by

$$\delta KE_j = \sqrt{\delta p_{Beam}^2 + \delta E_{Loss}^2 + \delta E_{\text{dep FF-j}}^2}, \quad (1.8)$$

572 where we have dropped the uncertainty on the mass, since it is orders of magnitude  
573 smaller than the other uncertainties. We assume the relative uncertainty on  $p_{Beam}$  to  
574 be 2%, and the uncertainty on the energy loss upstream to be 7 MeV, as calculated  
575 in Section 1.2.3. We describe the estimate of the uncertainty on  $E_{FF-j}$  in the rest of  
576 this section.

577 The energy deposited from the TPC front face until the  $j^{\text{th}}$  slice is the sum of the



578 measured energy deposited in each previous slabs  $E_i$ , i.e.

$$E_{\text{FF-j}} = \sum_{i < j} E_i, \quad (1.9)$$

579 where  $E_i$  is measured in each slab as the product of the stopping power,  $dE/dX_i$ ,  
 580 and the track pitch,  $Pitch_i$ , for that point. If we assume conservatively that the  
 581 measurements of  $E_i$  are not independent from one another, the uncertainty on  $E_{\text{FF-j}}$   
 582 becomes

$$\delta E_{\text{FF-j}} = (j - 1)\delta E_i, \quad (1.10)$$

583 where  $\delta E_i$  is the uncertainty on the energy loss in one slab of argon.

584 Figure 1.15 shows the distribution of the energy deposited in each slab of argon,  
 585 for the 60A negative pion dataset in black and for the pion only MC in blue. The  
 586 distributions are fitted with a landau displayed in red for data and in teal for MC.  
 587 The uncertainty on  $E_i$  is given by the width of the Landau fit to the data. A small  
 588 systematic uncertainty is given by a 1.0% difference between the most probable value  
 589 of the landau fits in data and MC.

590 So the uncertainty on the incident kinetic energy is given by

$$\delta K E^{\text{Incident}} = \sqrt{(\delta K E_{\text{Initial}})^2 + (\delta E_j^{\text{Slab}})^2} = \sqrt{(12\text{MeV})^2 + (2\text{MeV})^2} = 12.1\text{MeV} \quad (1.11)$$

591 Figure 1.16 shows the stacked version of the Energy Deposited plots with the  
 592 backgrounds stacked. The backgrounds are given in the ratio of 68.8% pion, 4.6%  
 593 muon, and 26.6% electron. Once they are taken in these ratios, the sum of the MC  
 594 is normalized to the sum of the data.

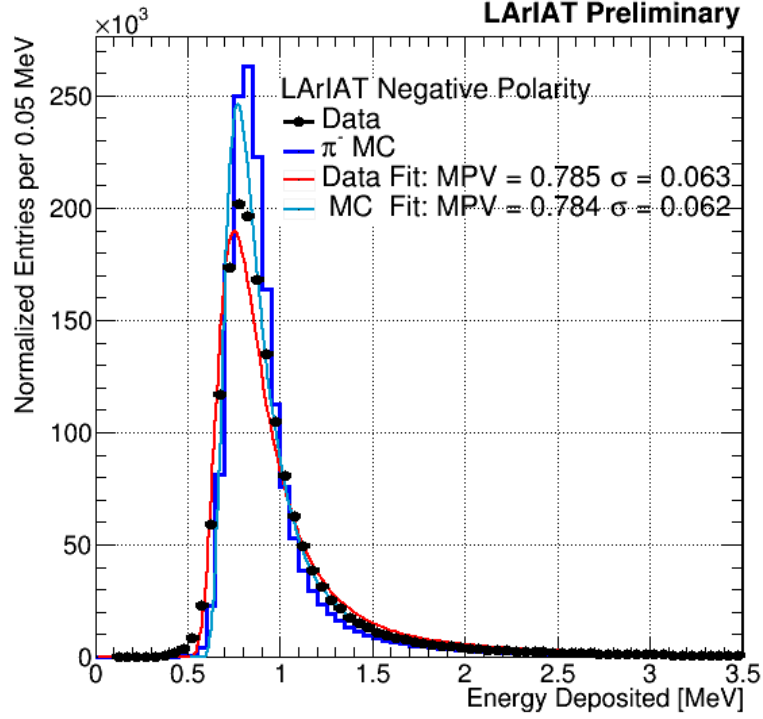


Figure 1.15: Energy Deposited in Pion MC and 60A data.

595 The energy at the interacting point is given by

$$KE_{Interaction} = \sqrt{P_{WCTrk}^2 + m_{\pi}^2} - E_{Loss} - (\Sigma dE/dX_i \times Pitch) \quad (1.12)$$

596 and has the exact same uncertainty as the incident kinetic energy plot. Thus these  
 597 estimates can be applied to getting the uncertainty on the energy of the reconstructed  
 598 cross-section.

599 A study we did was to look at the difference between DATA/MC in the dE/dX  
 600 and energy deposited. We basically found there is very little difference between the  
 601 two and we try to quantify how much the difference is.

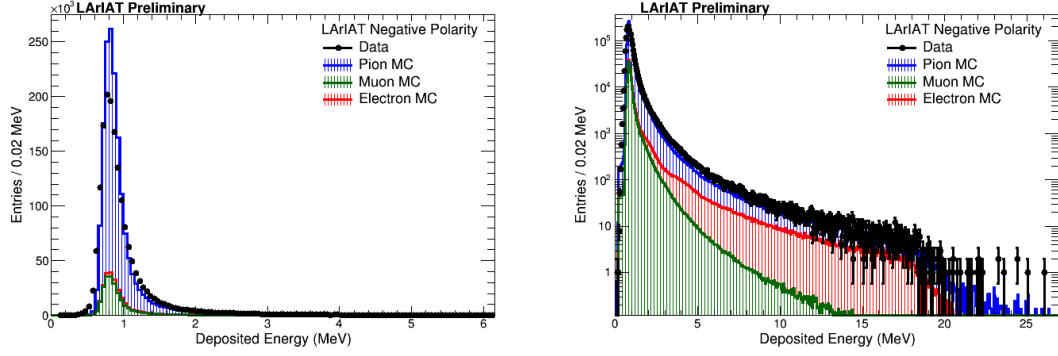


Figure 1.16: Energy Deposited with all the MC and 60A data.

### 1.4.3 $dE/dX$

Figure 1.17 shows the output of the fit of the Pion MC and the 60 Amp data. The MC is normalized to the data and both are fit to a Landau function.<sup>2</sup>

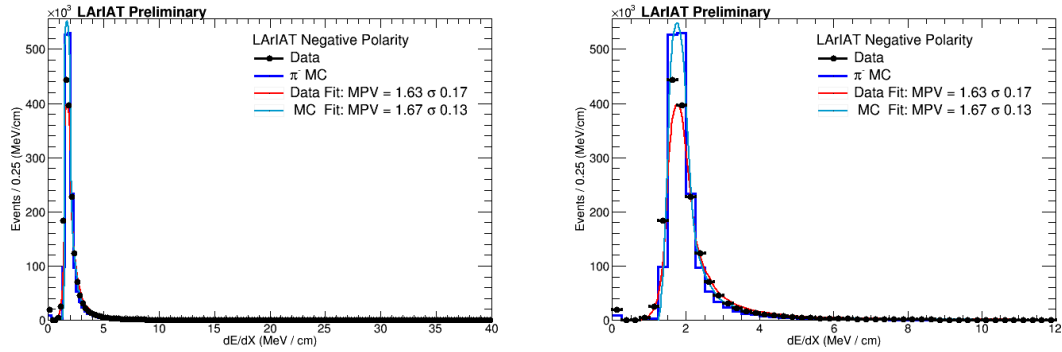


Figure 1.17:  $dE/dX$  for 60Amp data and data driven pion MC, both fit with a Landau

The difference between the two MPV's, is 2.4% between the data and the MC.

Figure 1.18 shows the stacked version of the  $dE/dX$  with the backgrounds stacked. The backgrounds are given in the ratio of 68.8% pion, 4.6% muon, and 26.6% electron. Once they are taken in these ratios, the sum of the MC is normalized to the sum of the data.

For completeness, the log scale versions of are shown in Figure 1.19.

Plotting scripts can be found here on [laratgpvm](https://laratgpvm.github.io)

<sup>2</sup>. The entries at  $dE/dX = 0$  come from an uninitialized variable and can/should be taken out of these plots

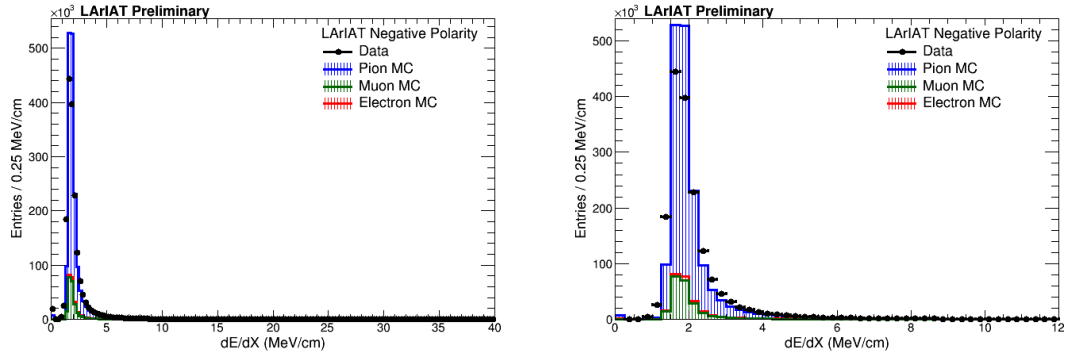


Figure 1.18: Stacked versions of the  $dE/dX$  with the data and electron/muon/pion MC.

612 `/lariat/app/users/jasaadi/v06_34_01_PionWeek/PlottingScripts`

613 and the samples were put here

614 `/lariat/data/users/elenag/theFinalPions/TPCDATA`

615

616 `/lariat/data/users/elenag/theFinalPions/TPC_MC/`

## 617 1.4.4 Energy Deposited

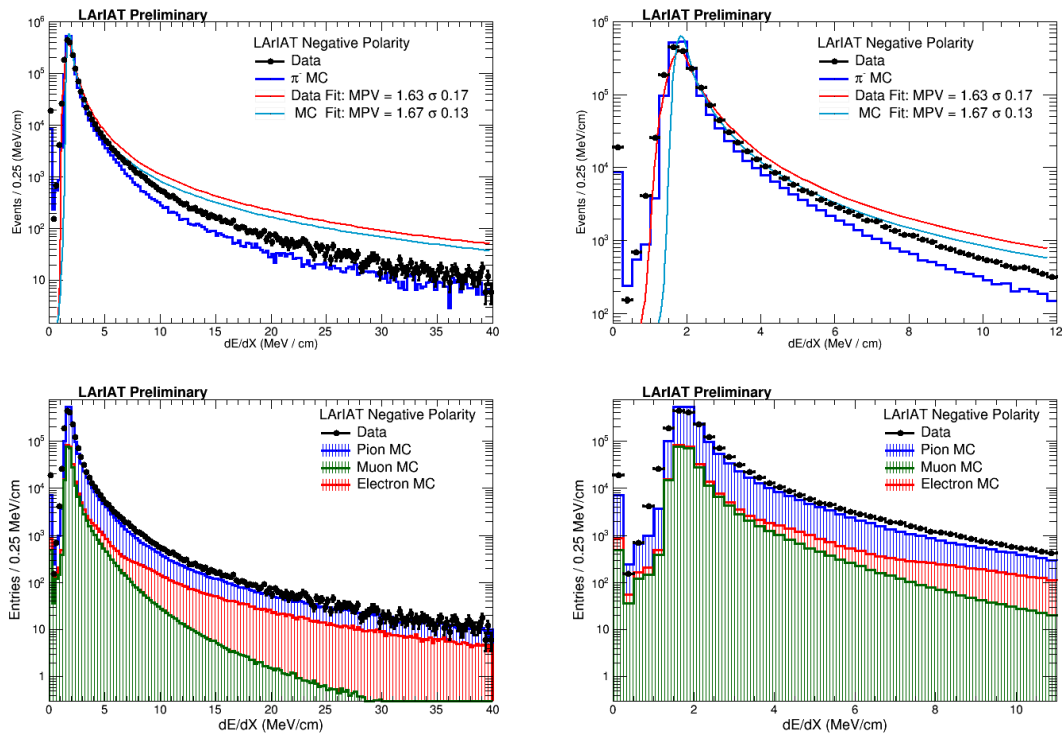


Figure 1.19:  $dE/dX$  for 60Amp data and MC shown in log scale

## Chapter 2

# Negative Pion Cross Section Measurement

### 2.1 Raw Cross Section

We measure the ( $\pi^-$ -Ar) cross section as a function of the kinetic energy in the two chosen data sets, the 60A and 100A negative runs. As will be clarified in 2.2, the corrections to the raw cross section depend on the beam conditions and need to proceed independently for the two data sets. Thus, we present here the two measurements separately.

As stated in section 0.3.2, the raw cross section is given by the equation

$$\sigma_{TOT}(E_i) = \frac{1}{n\delta X} \frac{N_{Interacting}(E_i)}{N_{Incident}(E_i)}. \quad (2.1)$$

where  $N_{Interacting}$  is the number of particles interacting in an argon slice at kinetic energy  $E_i$ ,  $N_{Incident}$  is number of particles incident on the argon slice at kinetic energy  $E_i$ ,  $n$  is the density of the target centers and  $\delta X$  is the thickness of the argon slice.

Figure 2.1 shows the interacting histogram for the 60A dataset on the left and for the 100A dataset on the right. Figure 2.2 shows the incident histogram for the 60A

dataset on the left and for the 100A dataset on the right. Figure 2.3 shows the raw cross section for the 60A dataset on the left and for the 100A dataset on the right. On all plots the same color scheme is used: the statistical uncertainty is shown in azure, while the systematic uncertainty is shown in blue. The calculation of the statistical uncertainty is laid out in section 2.1.1, while the systematics on this 2.1.2.

### 2.1.1 Statistical Uncertainty

The statistical uncertainty for each kinetic energy bin of the cross section plot is calculated by error propagation from the statistical uncertainty on  $N_{Incident}$  and  $N_{Interacting}$  correspondent bin. Since the number of incident hadrons in each energy bin is given by a simple counting, we assume that  $N_{Incident}$  is distributed as a poissonian with mean and  $\sigma^2$  equal to  $N_{Incident}$  in each bin. On the other hand,  $N_{Interacting}$  follows a binomial distribution: a particle in a given energy bin might or might not interact. The square of the variance for the binomial is given by

$$\sigma^2 = \mathcal{N} P_{Interacting} (1 - P_{Interacting}); \quad (2.2)$$

since the interaction probability  $P_{Interacting}$  is  $\frac{N_{Interacting}}{N_{Incident}}$  and the number of tries  $\mathcal{N}$  is  $N_{Incident}$ , equation 2.2 translates into

$$\sigma^2 = N_{Incident} \frac{N_{Interacting}}{N_{Incident}} \left(1 - \frac{N_{Interacting}}{N_{Incident}}\right) = N_{Interacting} \left(1 - \frac{N_{Interacting}}{N_{Incident}}\right). \quad (2.3)$$

$N_{Incident}$  and  $N_{Interacting}$  are not independent. The uncertainty on the cross section is thus calculated as

$$\delta\sigma_{tot}(E) = \sigma_{tot}(E) \left( \frac{\delta N_{Interacting}}{N_{Interacting}} + \frac{\delta N_{Incident}}{N_{Incident}} \right) \quad (2.4)$$

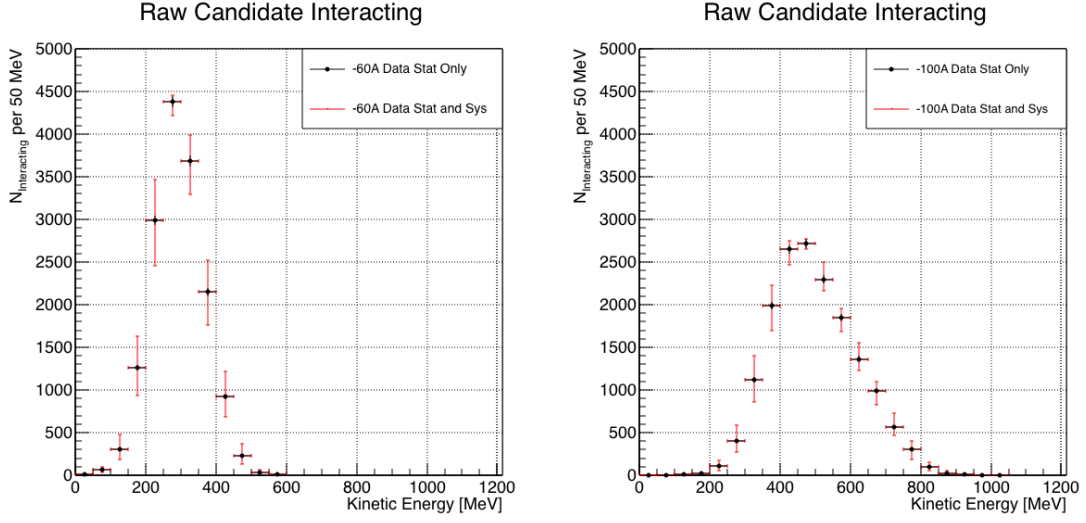


Figure 2.1: Raw number of interacting pion candidates as a function of the reconstructed kinetic energy for the 60A runs (lef) and for the 100A runs (right). The statistical uncertainties are shown in azure, the systematic uncertainties in blue.

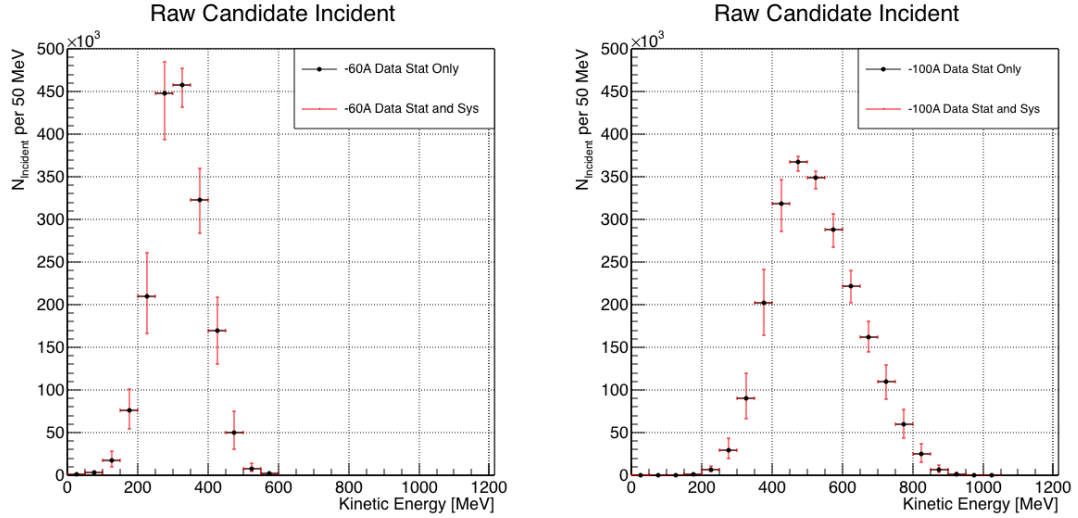


Figure 2.2: Raw number of incident pion candidates as a function of the reconstructed kinetic energy for the 60A runs (lef) and for the 100A runs (right). The statistical uncertainties are shown in azure, the systematic uncertainties in blue.



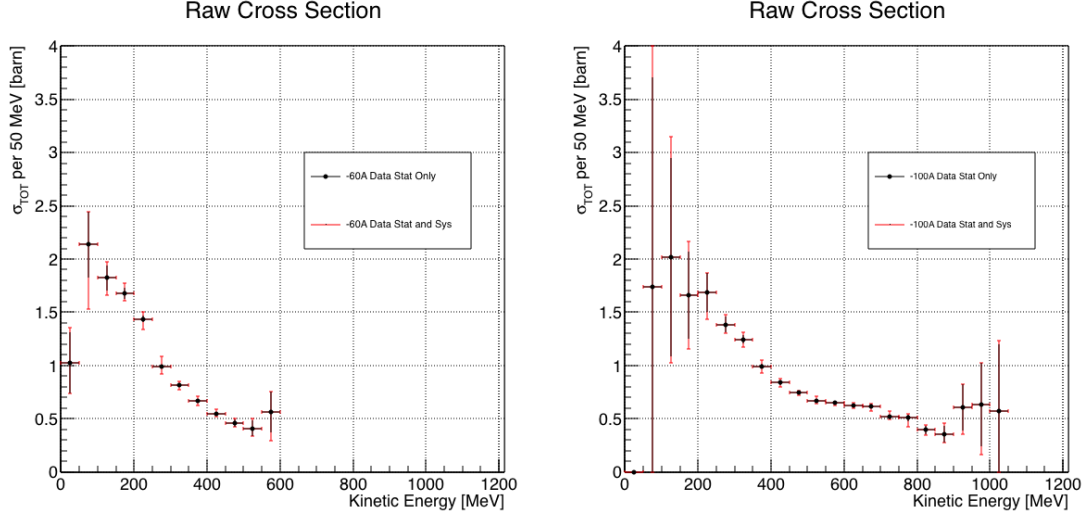


Figure 2.3: Raw ( $\pi^-$ -Ar) total hadronic cross section for the 60A runs (lef) and for the 100A runs (right). The statistical uncertainties are shown in azure, the systematic uncertainties in blue.

650 where:

$$\delta N_{Incident} = \sqrt{N_{Incident}} \quad (2.5)$$

$$\delta N_{Interacting} = \sqrt{N_{Interacting} \left( 1 - \frac{N_{Interacting}}{N_{Incident}} \right)}. \quad (2.6)$$

### 651 2.1.2 Treatment of Systematics

## 652 2.2 Corrections to the Raw Cross Section

### 653 2.2.1 Treatment of Systematics

# Bibliography

- [1] Precision electroweak measurements on the  $z$  resonance. *Physics Reports*, 427(5):257 – 454, 2006.
- [2] K. Abe, J. Amey, C. Andreopoulos, M. Antonova, S. Aoki, A. Ariga, D. Autiero, S. Ban, M. Barbi, G. J. Barker, G. Barr, C. Barry, P. Bartet-Friburg, M. Batkiewicz, V. Berardi, S. Berkman, S. Bhadra, S. Bienstock, A. Blondel, S. Bolognesi, S. Bordini, S. B. Boyd, D. Brailsford, A. Bravar, C. Bronner, M. Buizza Avanzini, R. G. Calland, T. Campbell, S. Cao, S. L. Cartwright, M. G. Catanesi, A. Cervera, C. Checchia, D. Cherdack, N. Chikuma, G. Christodoulou, A. Clifton, J. Coleman, G. Collazuol, D. Coplowe, A. Cudd, A. Dabrowska, G. De Rosa, T. Dealtry, P. F. Denner, S. R. Dennis, C. Densham, D. Dewhurst, F. Di Lodovico, S. Di Luise, S. Dolan, O. Drapier, K. E. Duffy, J. Dumarchez, M. Dziewiecki, S. Emery-Schrenk, A. Ereditato, T. Feusels, A. J. Finch, G. A. Fiorentini, M. Friend, Y. Fujii, D. Fukuda, Y. Fukuda, V. Galymov, A. Garcia, C. Giganti, F. Gizzarelli, T. Golan, M. Gonin, D. R. Hadley, L. Haegel, M. D. Haigh, D. Hansen, J. Harada, M. Hartz, T. Hasegawa, N. C. Hastings, T. Hayashino, Y. Hayato, R. L. Helmer, A. Hillairet, T. Hiraki, A. Hiramoto, S. Hirota, M. Hogan, J. Holeczek, F. Hosomi, K. Huang, A. K. Ichikawa, M. Ikeda, J. Imber, J. Insler, R. A. Intonti, T. Ishida, T. Ishii, E. Iwai, K. Iwamoto, A. Izmaylov, B. Jamieson, M. Jiang, S. Johnson, P. Jonsson, C. K. Jung, M. Kabirnezhad, A. C. Kaboth, T. Kajita, H. Kakuno, J. Kameda,

675 D. Karlen, T. Katori, E. Kearns, M. Khabibullin, A. Khotjantsev, H. Kim,  
 676 J. Kim, S. King, J. Kisiel, A. Knight, A. Knox, T. Kobayashi, L. Koch, T. Koga,  
 677 A. Konaka, K. Kondo, L. L. Kormos, A. Korzenev, Y. Koshio, K. Kowalik,  
 678 W. Kropp, Y. Kudenko, R. Kurjata, T. Kutter, J. Lagoda, I. Lamont, M. Lam-  
 679 oureux, E. Larkin, P. Lasorak, M. Laveder, M. Lawe, M. Licciardi, T. Lindner,  
 680 Z. J. Liptak, R. P. Litchfield, X. Li, A. Longhin, J. P. Lopez, T. Lou, L. Ludovici,  
 681 X. Lu, L. Magaletti, K. Mahn, M. Malek, S. Manly, A. D. Marino, J. F. Martin,  
 682 P. Martins, S. Martynenko, T. Maruyama, V. Matveev, K. Mavrokoridis, W. Y.  
 683 Ma, E. Mazzucato, M. McCarthy, N. McCauley, K. S. McFarland, C. McGrew,  
 684 A. Mefodiev, C. Metelko, M. Mezzetto, P. Mijakowski, A. Minamino, O. Mi-  
 685 neev, S. Mine, A. Missert, M. Miura, S. Moriyama, Th. A. Mueller, J. Myslik,  
 686 T. Nakadaira, M. Nakahata, K. G. Nakamura, K. Nakamura, K. D. Nakamura,  
 687 Y. Nakanishi, S. Nakayama, T. Nakaya, K. Nakayoshi, C. Nantais, C. Nielsen,  
 688 M. Nirkko, K. Nishikawa, Y. Nishimura, P. Novella, J. Nowak, H. M. O’Keeffe,  
 689 K. Okumura, T. Okusawa, W. Oryszczak, S. M. Oser, T. Ovsyannikova, R. A.  
 690 Owen, Y. Oyama, V. Palladino, J. L. Palomino, V. Paolone, N. D. Patel,  
 691 P. Paudyal, M. Pavin, D. Payne, J. D. Perkin, Y. Petrov, L. Pickard, L. Pick-  
 692 ering, E. S. Pinzon Guerra, C. Pistillo, B. Popov, M. Posiadala-Zezula, J.-M.  
 693 Poutissou, R. Poutissou, P. Przewlocki, B. Quilain, T. Radermacher, E. Radi-  
 694 cioni, P. N. Ratoff, M. Ravonel, M. A. Rayner, A. Redij, E. Reinherz-Aronis,  
 695 C. Riccio, P. A. Rodrigues, E. Rondio, B. Rossi, S. Roth, A. Rubbia, A. Rychter,  
 696 K. Sakashita, F. Sánchez, E. Scantamburlo, K. Scholberg, J. Schwehr, M. Scott,  
 697 Y. Seiya, T. Sekiguchi, H. Sekiya, D. Sgalaberna, R. Shah, A. Shaikhiev,  
 698 F. Shaker, D. Shaw, M. Shiozawa, T. Shirahige, S. Short, M. Smy, J. T.  
 699 Sobczyk, H. Sobel, M. Sorel, L. Southwell, J. Steinmann, T. Stewart, P. Stowell,  
 700 Y. Suda, S. Suvorov, A. Suzuki, S. Y. Suzuki, Y. Suzuki, R. Tacik, M. Tada,  
 701 A. Takeda, Y. Takeuchi, H. K. Tanaka, H. A. Tanaka, D. Terhorst, R. Terri,

702 T. Thakore, L. F. Thompson, S. Tobayama, W. Toki, T. Tomura, C. Tourama-  
 703 nis, T. Tsukamoto, M. Tzanov, Y. Uchida, M. Vagins, Z. Vallari, G. Vasseur,  
 704 T. Vladisavljevic, T. Wachala, C. W. Walter, D. Wark, M. O. Wascko, A. We-  
 705 ber, R. Wendell, R. J. Wilkes, M. J. Wilking, C. Wilkinson, J. R. Wilson, R. J.  
 706 Wilson, C. Wret, Y. Yamada, K. Yamamoto, M. Yamamoto, C. Yanagisawa,  
 707 T. Yano, S. Yen, N. Yershov, M. Yokoyama, K. Yoshida, T. Yuan, M. Yu, A. Za-  
 708 lewska, J. Zalipska, L. Zambelli, K. Zaremba, M. Ziembicki, E. D. Zimmerman,  
 709 M. Zito, and J. Żmuda. Combined analysis of neutrino and antineutrino oscil-  
 710 lations at t2k. *Phys. Rev. Lett.*, 118:151801, Apr 2017.

711 [3] K. Abe, Y. Haga, Y. Hayato, M. Ikeda, K. Iyogi, J. Kameda, Y. Kishimoto,  
 712 M. Miura, S. Moriyama, M. Nakahata, T. Nakajima, Y. Nakano, S. Nakayama,  
 713 A. Orii, H. Sekiya, M. Shiozawa, A. Takeda, H. Tanaka, T. Tomura, R. A. Wen-  
 714 dell, R. Akutsu, T. Irvine, T. Kajita, K. Kaneyuki, Y. Nishimura, E. Richard,  
 715 K. Okumura, L. Labarga, P. Fernandez, J. Gustafson, C. Kachulis, E. Kearns,  
 716 J. L. Raaf, J. L. Stone, L. R. Sulak, S. Berkman, C. M. Nantais, H. A.  
 717 Tanaka, S. Tobayama, M. Goldhaber, W. R. Kropp, S. Mine, P. Weatherly,  
 718 M. B. Smy, H. W. Sobel, V. Takhistov, K. S. Ganezer, B. L. Hartfiel, J. Hill,  
 719 N. Hong, J. Y. Kim, I. T. Lim, R. G. Park, A. Himmel, Z. Li, E. O’Sullivan,  
 720 K. Scholberg, C. W. Walter, T. Wongjirad, T. Ishizuka, S. Tasaka, J. S. Jang,  
 721 J. G. Learned, S. Matsuno, S. N. Smith, M. Friend, T. Hasegawa, T. Ishida,  
 722 T. Ishii, T. Kobayashi, T. Nakadaira, K. Nakamura, Y. Oyama, K. Sakashita,  
 723 T. Sekiguchi, T. Tsukamoto, A. T. Suzuki, Y. Takeuchi, T. Yano, S. V. Cao,  
 724 T. Hiraki, S. Hirota, K. Huang, T. Kikawa, A. Minamino, T. Nakaya, K. Suzuki,  
 725 Y. Fukuda, K. Choi, Y. Itow, T. Suzuki, P. Mijakowski, K. Frankiewicz, J. Hig-  
 726 night, J. Imber, C. K. Jung, X. Li, J. L. Palomino, M. J. Wilking, C. Yanag-  
 727 isawa, D. Fukuda, H. Ishino, T. Kayano, A. Kibayashi, Y. Koshio, T. Mori,  
 728 M. Sakuda, C. Xu, Y. Kuno, R. Tacik, S. B. Kim, H. Okazawa, Y. Choi,

729 K. Nishijima, M. Koshiha, Y. Totsuka, Y. Suda, M. Yokoyama, C. Bronner,  
730 M. Hartz, K. Martens, Ll. Marti, Y. Suzuki, M. R. Vagins, J. F. Martin, A. Kon-  
731 aka, S. Chen, Y. Zhang, and R. J. Wilkes. Search for proton decay via  $p \rightarrow e^+ \pi^0$   
732 and  $p \rightarrow \mu^+ \pi^0$  in 0.31 megaton  $\cdot$  years exposure of the super-kamiokande water  
733 cherenkov detector. *Phys. Rev. D*, 95:012004, Jan 2017.

734 [4] R Acciarri, C Adams, J Asaadi, B Baller, T Bolton, C Bromberg, F Ca-  
735 vanna, E Church, D Edmunds, A Ereditato, S Farooq, B Fleming, H Greenlee,  
736 G Horton-Smith, C James, E Klein, K Lang, P Laurens, D McKee, R Mehdiyev,  
737 B Page, O Palamara, K Partyka, G Rameika, B Rebel, M Soderberg, J Spitz,  
738 A M Szelc, M Weber, M Wojcik, T Yang, and G P Zeller. A study of electron  
739 recombination using highly ionizing particles in the argoneut liquid argon tpc.  
740 *Journal of Instrumentation*, 8(08):P08005, 2013.

741 [5] R Acciarri, M Antonello, B Baibussinov, M Baldo-Ceolin, P Benetti,  
742 F Calaprice, E Calligarich, M Cambiaghi, N Canci, F Carbonara, F Cavanna,  
743 S Centro, A G Cocco, F Di Pompeo, G Fiorillo, C Galbiati, V Gallo, L Grandi,  
744 G Meng, I Modena, C Montanari, O Palamara, L Pandola, G B Piano Mortari,  
745 F Pietropaolo, G L Raselli, M Roncadelli, M Rossella, C Rubbia, E Segreto,  
746 A M Szelc, S Ventura, and C Vignoli. Effects of nitrogen contamination in  
747 liquid argon. *Journal of Instrumentation*, 5(06):P06003, 2010.

748 [6] R. Acciarri et al. Demonstration and Comparison of Operation of Photomulti-  
749 plier Tubes at Liquid Argon Temperature. *JINST*, 7:P01016, 2012.

750 [7] R. Acciarri et al. Design and Construction of the MicroBooNE Detector. *JINST*,  
751 12(02):P02017, 2017.

752 [8] R. Acciarri et al. First Observation of Low Energy Electron Neutrinos in a  
753 Liquid Argon Time Projection Chamber. *Phys. Rev.*, D95(7):072005, 2017.

754 [Phys. Rev.D95,072005(2017)].

755 [9] M Adamowski, B Carls, E Dvorak, A Hahn, W Jaskierny, C Johnson, H Jostlein,  
756 C Kendziora, S Lockwitz, B Pahlka, R Plunkett, S Pordes, B Rebel, R Schmitt,  
757 M Stancari, T Tope, E Voirin, and T Yang. The liquid argon purity demon-  
758 strator. *Journal of Instrumentation*, 9(07):P07005, 2014.

759 [10] C. Adams et al. The Long-Baseline Neutrino Experiment: Exploring Funda-  
760 mental Symmetries of the Universe. 2013.

761 [11] P. Adamson, L. Aliaga, D. Ambrose, N. Anfimov, A. Antoshkin, E. Arrieta-  
762 Diaz, K. Augsten, A. Aurisano, C. Backhouse, M. Baird, B. A. Bambah,  
763 K. Bays, B. Behera, S. Bending, R. Bernstein, V. Bhatnagar, B. Bhuyan,  
764 J. Bian, T. Blackburn, A. Bolshakova, C. Bromberg, J. Brown, G. Brunetti,  
765 N. Buchanan, A. Butkevich, V. Bychkov, M. Campbell, E. Catano-Mur, S. Chil-  
766 dress, B. C. Choudhary, B. Chowdhury, T. E. Coan, J. A. B. Coelho, M. Colo,  
767 J. Cooper, L. Corwin, L. Cremonesi, D. Cronin-Hennessy, G. S. Davies, J. P.  
768 Davies, P. F. Derwent, R. Dharmapalan, P. Ding, Z. Djurcic, E. C. Dukes,  
769 H. Duyang, S. Edayath, R. Ehrlich, G. J. Feldman, M. J. Frank, M. Gabrielyan,  
770 H. R. Gallagher, S. Germani, T. Ghosh, A. Giri, R. A. Gomes, M. C. Goodman,  
771 V. Grichine, R. Group, D. Grover, B. Guo, A. Habig, J. Hartnell, R. Hatcher,  
772 A. Hatzikoutelis, K. Heller, A. Himmel, A. Holin, J. Hylen, F. Jediny, M. Judah,  
773 G. K. Kafka, D. Kalra, S. M. S. Kasahara, S. Kasetti, R. Keloth, L. Kolupaeva,  
774 S. Kotelnikov, I. Kourbanis, A. Kreymer, A. Kumar, S. Kurbanov, K. Lang,  
775 W. M. Lee, S. Lin, J. Liu, M. Lokajicek, J. Lozier, S. Luchuk, K. Maan, S. Mag-  
776 ill, W. A. Mann, M. L. Marshak, K. Matera, V. Matveev, D. P. Méndez, M. D.  
777 Messier, H. Meyer, T. Miao, W. H. Miller, S. R. Mishra, R. Mohanta, A. Moren,  
778 L. Mualem, M. Muether, S. Mufson, R. Murphy, J. Musser, J. K. Nelson,  
779 R. Nichol, E. Niner, A. Norman, T. Nosek, Y. Oksuzian, A. Olshevskiy, T. Ol-

son, J. Paley, P. Pandey, R. B. Patterson, G. Pawloski, D. Pershey, O. Petrova,  
R. Petti, S. Phan-Budd, R. K. Plunkett, R. Poling, B. Potukuchi, C. Principato,  
F. Psihas, A. Radovic, R. A. Rameika, B. Rebel, B. Reed, D. Rocco, P. Rojas,  
V. Ryabov, K. Sachdev, P. Sail, O. Samoylov, M. C. Sanchez, R. Schroeter,  
J. Sepulveda-Quiroz, P. Shanahan, A. Sheshukov, J. Singh, J. Singh, P. Singh,  
V. Singh, J. Smolik, N. Solomey, E. Song, A. Sousa, K. Soustruznik, M. Strait,  
L. Suter, R. L. Talaga, M. C. Tamsett, P. Tas, R. B. Thayyullathil, J. Thomas,  
X. Tian, S. C. Tognini, J. Tripathi, A. Tsaris, J. Urheim, P. Vahle, J. Vassel,  
L. Vinton, A. Vold, T. Vrba, B. Wang, M. Wetstein, D. Whittington, S. G. Wo-  
jcicki, J. Wolcott, N. Yadav, S. Yang, J. Zalesak, B. Zamorano, and R. Zwaska.  
Constraints on oscillation parameters from  $\nu_e$  appearance and  $\nu_\mu$  disappearance  
in nova. *Phys. Rev. Lett.*, 118:231801, Jun 2017.

[12] Alan Agresti. *Categorical Data Analysis*. Wiley Series in Probability and Statis-  
tics. Wiley, 2013.

[13] A. Aguilar-Arevalo et al. Evidence for neutrino oscillations from the observation  
of anti-neutrino(electron) appearance in a anti-neutrino(muon) beam. *Phys.*  
*Rev.*, D64:112007, 2001.

[14] A. A. Aguilar-Arevalo et al. Improved Search for  $\bar{\nu}_\mu \rightarrow \bar{\nu}_e$  Oscillations in the  
MiniBooNE Experiment. *Phys. Rev. Lett.*, 110:161801, 2013.

[15] S. Amoruso et al. Study of electron recombination in liquid argon with the  
ICARUS TPC. *Nucl. Instrum. Meth.*, A523:275–286, 2004.

[16] C. Anderson et al. The ArgoNeuT Detector in the NuMI Low-Energy beam  
line at Fermilab. *JINST*, 7:P10019, 2012.

[17] C. Andreopoulos et al. The GENIE Neutrino Monte Carlo Generator. *Nucl.*  
*Instrum. Meth.*, A614:87–104, 2010.

- [18] Timofei Bolshakov Andrey Petrov. Java synoptic toolkit. Technical report, Sept 2010.
- [19] M. Antonello, B. Baibussinov, P. Benetti, E. Calligarich, N. Canci, S. Centro, A. Cesana, K. Cieslik, D. B. Cline, A. G. Cocco, A. Dabrowska, D. Dequal, A. Dermenev, R. Dolfini, C. Farnese, A. Fava, A. Ferrari, G. Fiorillo, D. Gibin, S. Gninenko, A. Guglielmi, M. Haranczyk, J. Holeczek, A. Ivashkin, J. Kisiel, I. Kochanek, J. Lagoda, S. Mania, A. Menegolli, G. Meng, C. Montanari, S. Otwinowski, A. Piazzoli, P. Picchi, F. Pietropaolo, P. Plonski, A. Rappoldi, G. L. Raselli, M. Rossella, C. Rubbia, P. Sala, A. Scaramelli, E. Segreto, F. Sergiampietri, D. Stefan, J. Stepaniak, R. Sulej, M. Szarska, M. Terani, F. Varanini, S. Ventura, C. Vignoli, H. Wang, X. Yang, A. Zalewska, and K. Zaremba. Precise 3d track reconstruction algorithm for the ICARUS t600 liquid argon time projection chamber detector. *Advances in High Energy Physics*, 2013:1–16, 2013.
- [20] M. Antonello et al. A Proposal for a Three Detector Short-Baseline Neutrino Oscillation Program in the Fermilab Booster Neutrino Beam. 2015.
- [21] D. Ashery, I. Navon, G. Azuelos, H. K. Walter, H. J. Pfeiffer, and F. W. Schlepütz. True absorption and scattering of pions on nuclei. *Phys. Rev. C*, 23:2173–2185, May 1981.
- [22] C. Athanassopoulos et al. Evidence for  $\nu(\mu) \rightarrow \nu(e)$  neutrino oscillations from LSND. *Phys. Rev. Lett.*, 81:1774–1777, 1998.
- [23] Borut Bajc, Junji Hisano, Takumi Kuwahara, and Yuji Omura. Threshold corrections to dimension-six proton decay operators in non-minimal  $\{\text{SUSY}\}$   $\text{su}(5)$   $\{\text{GUTs}\}$ . *Nuclear Physics B*, 910:1 – 22, 2016.
- [24] B. Baller. Trajcluster user guide. Technical report, apr 2016.



- [25] Gary Barker. Neutrino event reconstruction in a liquid argon TPC. *Journal of Physics: Conference Series*, 308:012015, jul 2011.
- [26] BASF Corp. 100 Park Avenue, Florham Park, NJ 07932 USA.
- [27] R. Becker-Szendy, C. B. Bratton, D. R. Cady, D. Casper, R. Claus, M. Crouch, S. T. Dye, W. Gajewski, M. Goldhaber, T. J. Haines, P. G. Halverson, T. W. Jones, D. Kielczewska, W. R. Kropp, J. G. Learned, J. M. LoSecco, C. McGrew, S. Matsuno, J. Matthews, M. S. Mudah, L. Price, F. Reines, J. Schultz, D. Sinclair, H. W. Sobel, J. L. Stone, L. R. Sulak, R. Svoboda, G. Thornton, and J. C. van der Velde. Search for proton decay into  $e^+ + \pi^0$  in the imb-3 detector. *Phys. Rev. D*, 42:2974–2976, Nov 1990.
- [28] J B Birks. Scintillations from organic crystals: Specific fluorescence and relative response to different radiations. *Proceedings of the Physical Society. Section A*, 64(10):874, 1951.
- [29] A. Bodek and J. L. Ritchie. Further studies of fermi-motion effects in lepton scattering from nuclear targets. *Phys. Rev. D*, 24:1400–1402, Sep 1981.
- [30] Mark G. Boulay and A. Hime. Direct WIMP detection using scintillation time discrimination in liquid argon. 2004.
- [31] D. V. Bugg, R. S. Gilmore, K. M. Knight, D. C. Salter, G. H. Stafford, E. J. N. Wilson, J. D. Davies, J. D. Dowell, P. M. Hattersley, R. J. Homer, A. W. O’dell, A. A. Carter, R. J. Tapper, and K. F. Riley. Kaon-nucleon total cross sections from 0.6 to 2.65 gev/  $c$ . *Phys. Rev.*, 168:1466–1475, Apr 1968.
- [32] W. M. Burton and B. A. Powell. Fluorescence of tetraphenyl-butadiene in the vacuum ultraviolet. *Applied Optics*, 12(1):87, jan 1973.
- [33] CAEN. Caen v1495 data sheet. Technical report, jan 2018.

- [34] CAEN. Caen v1740 data sheet. Technical report, jan 2018.
- [35] A. S. Carroll, I. H. Chiang, C. B. Dover, T. F. Kycia, K. K. Li, P. O. Mazur, D. N. Michael, P. M. Mockett, D. C. Rahm, and R. Rubinstein. Pion-nucleus total cross sections in the (3,3) resonance region. *Phys. Rev. C*, 14:635–638, Aug 1976.
- [36] D. Casper. The nuance neutrino physics simulation, and the future. *Nuclear Physics B - Proceedings Supplements*, 112(1-3):161–170, nov 2002.
- [37] A. Cervera, A. Donini, M.B. Gavela, J.J. Gomez Cadenas, P. Hernández, O. Mena, and S. Rigolin. Golden measurements at a neutrino factory. *Nuclear Physics B*, 579(1-2):17–55, jul 2000.
- [38] E. Church. LArSoft: A Software Package for Liquid Argon Time Projection Drift Chambers. 2013.
- [39] ATLAS Collaboration. Observation of a new particle in the search for the standard model higgs boson with the ATLAS detector at the LHC. *Physics Letters B*, 716(1):1–29, sep 2012.
- [40] CMS Collaboration. Observation of a new boson at a mass of 125 gev with the cms experiment at the lhc. *Physics Letters B*, 716(1):30 – 61, 2012.
- [41] The LArIAT Collaboration. The liquid argon in a testbeam (lariat) experiment. Technical report, In Preparation 2018.
- [42] Stefano Dell’Oro, Simone Marcocci, Matteo Viel, and Francesco Vissani. Neutrinoless double beta decay: 2015 review. *Advances in High Energy Physics*, 2016:1–37, 2016.

- [43] S.E. Derenzo, A.R. Kirschbaum, P.H. Eberhard, R.R. Ross, and F.T. Solmitz. Test of a liquid argon chamber with 20 m rms resolution. *Nuclear Instruments and Methods*, 122:319 – 327, 1974.
- [44] Savas Dimopoulos, Stuart Raby, and Frank Wilczek. Proton Decay in Supersymmetric Models. *Phys. Lett.*, B112:133, 1982.
- [45] D. Drakoulakos et al. Proposal to perform a high-statistics neutrino scattering experiment using a fine-grained detector in the NuMI beam. 2004.
- [46] A Ereditato, C C Hsu, S Janos, I Kreslo, M Messina, C Rudolf von Rohr, B Rossi, T Strauss, M S Weber, and M Zeller. Design and operation of argontube: a 5 m long drift liquid argon tpc. *Journal of Instrumentation*, 8(07):P07002, 2013.
- [47] Torleif Ericson and Wolfram Weise. *Pions and Nuclei (The International Series of Monographs on Physics)*. Oxford University Press, 1988.
- [48] A.A. Aguilar-Arevalo et al. The miniboone detector. *Nuclear Instruments and Methods in Physics Research Section A: Accelerators, Spectrometers, Detectors and Associated Equipment*, 599(1):28 – 46, 2009.
- [49] Antonio Bueno et al. Nucleon decay searches with large liquid argon TPC detectors at shallow depths: atmospheric neutrinos and cosmogenic backgrounds. *Journal of High Energy Physics*, 2007(04):041–041, apr 2007.
- [50] A.S. Clough et al. Pion-nucleus total cross sections from 88 to 860 MeV. *Nuclear Physics B*, 76(1):15–28, jul 1974.
- [51] B.W. Allardyce et al. Pion reaction cross sections and nuclear sizes. *Nuclear Physics A*, 209(1):1 – 51, 1973.

- [52] C Athanassopoulos et al. The liquid scintillator neutrino detector and LAMPF neutrino source. *Nuclear Instruments and Methods in Physics Research Section A: Accelerators, Spectrometers, Detectors and Associated Equipment*, 388(1-2):149–172, mar 1997.
- [53] F. Binon et al. Scattering of negative pions on carbon. *Nuclear Physics B*, 17(1):168 – 188, 1970.
- [54] L. Aliaga et al. Minerva neutrino detector response measured with test beam data. *Nuclear Instruments and Methods in Physics Research Section A: Accelerators, Spectrometers, Detectors and Associated Equipment*, 789:28 – 42, 2015.
- [55] M Adamowski et al. The liquid argon purity demonstrator. *Journal of Instrumentation*, 9(07):P07005, 2014.
- [56] P. Vilain et al. Coherent single charged pion production by neutrinos. *Physics Letters B*, 313(1-2):267–275, aug 1993.
- [57] R. Acciarri et al. Convolutional neural networks applied to neutrino events in a liquid argon time projection chamber. *Journal of Instrumentation*, 12(03):P03011, 2017.
- [58] R. Acciarri et al. Design and construction of the MicroBooNE detector. *Journal of Instrumentation*, 12(02):P02017–P02017, feb 2017.
- [59] C. E. Aalseth et al. DarkSide-20k: A 20 tonne two-phase LAr TPC for direct dark matter detection at LNGS. *The European Physical Journal Plus*, 133(3), mar 2018.
- [60] H Fenker. Standard beam pwc for fermilab. Technical report, Fermi National Accelerator Lab., Batavia, IL (USA), 1983.

- 923 [61] H Fesbach. Theoretical nuclear physics: Nuclear reactions. 1992.
- 924 [62] J. A. Formaggio and G. P. Zeller. From ev to eev: Neutrino cross sections across  
925 energy scales. *Rev. Mod. Phys.*, 84:1307–1341, Sep 2012.
- 926 [63] E. Friedman et al. K+ nucleus reaction and total cross-sections: New analysis  
927 of transmission experiments. *Phys. Rev.*, C55:1304–1311, 1997.
- 928 [64] V.M. Gehman, S.R. Seibert, K. Rielage, A. Hime, Y. Sun, D.-M. Mei,  
929 J. Maassen, and D. Moore. Fluorescence efficiency and visible re-emission  
930 spectrum of tetraphenyl butadiene films at extreme ultraviolet wavelengths.  
931 *Nuclear Instruments and Methods in Physics Research Section A: Accelerators,*  
932 *Spectrometers, Detectors and Associated Equipment*, 654(1):116 – 121, 2011.
- 933 [65] H. Geiger and E. Marsden. On a diffuse reflection of the formula-particles.  
934 *Proceedings of the Royal Society A: Mathematical, Physical and Engineering*  
935 *Sciences*, 82(557):495–500, jul 1909.
- 936 [66] Howard Georgi and S. L. Glashow. Unity of all elementary-particle forces. *Phys.*  
937 *Rev. Lett.*, 32:438–441, Feb 1974.
- 938 [67] D.Y. Wong (editor) G.L. Shaw (Editor). *Pion-nucleon Scattering*. John Wiley  
939 & Sons Inc, 1969.
- 940 [68] Glassman High Voltage, Inc., Precision Regulated High Voltage DC Power Sup-  
941 ply.
- 942 [69] D S Gorbunov. Sterile neutrinos and their role in particle physics and cosmology.  
943 *Physics-Uspekhi*, 57(5):503, 2014.
- 944 [70] C. Green, J. Kowalkowski, M. Paterno, M. Fischler, L. Garren, and Q. Lu. The  
945 Art Framework. *J. Phys. Conf. Ser.*, 396:022020, 2012.

- [71] S. Hansen, D. Jensen, G. Savage, E. Skup, and A. Soha. Fermilab test beam multi-wire proportional chamber tracking system upgrade. June 2014. International Conference on Technology and Instrumentation in Particle Physics (TIPP 2014).
- [72] J. Harada. Non-maximal  $\theta_{23}$ , large  $\theta_{13}$  and tri-bimaximal  $\theta_{12}$  via quark-lepton complementarity at next-to-leading order. *EPL (Europhysics Letters)*, 103(2):21001, 2013.
- [73] Peter W. Higgs. Broken symmetries and the masses of gauge bosons. *Physical Review Letters*, 13(16):508–509, oct 1964.
- [74] P.W. Higgs. Broken symmetries, massless particles and gauge fields. *Physics Letters*, 12(2):132–133, sep 1964.
- [75] H J Hilke. Time projection chambers. *Reports on Progress in Physics*, 73(11):116201, 2010.
- [76] N. Ishida, M. Chen, T. Doke, K. Hasuike, A. Hitachi, M. Gaudreau, M. Kase, Y. Kawada, J. Kikuchi, T. Komiyama, K. Kuwahara, K. Masuda, H. Okada, Y.H. Qu, M. Suzuki, and T. Takahashi. Attenuation length measurements of scintillation light in liquid rare gases and their mixtures using an improved reflection suppresser. *Nuclear Instruments and Methods in Physics Research Section A: Accelerators, Spectrometers, Detectors and Associated Equipment*, 384(2-3):380–386, jan 1997.
- [77] George Jaffé. Zur theorie der ionisation in kolonnen. *Annalen der Physik*, 347(12):303–344, 1913.
- [78] C. Jarlskog. A basis independent formulation of the connection between quark mass matrices, CP violation and experiment. *Zeitschrift für Physik C Particles and Fields*, 29(3):491–497, sep 1985.

- [79] B J P Jones, C S Chiu, J M Conrad, C M Ignarra, T Katori, and M Toups. A measurement of the absorption of liquid argon scintillation light by dissolved nitrogen at the part-per-million level. *Journal of Instrumentation*, 8(07):P07011, 2013.
- [80] Benjamin J. P. Jones. *Sterile Neutrinos in Cold Climates*. PhD thesis, MIT, 2015.
- [81] Cezary Juszczak, Jarosław A. Nowak, and Jan T. Sobczyk. Simulations from a new neutrino event generator. *Nuclear Physics B - Proceedings Supplements*, 159:211–216, sep 2006.
- [82] D. I. Kazakov. Beyond the standard model: In search of supersymmetry. In *2000 European School of high-energy physics, Caramulo, Portugal, 20 Aug-2 Sep 2000: Proceedings*, pages 125–199, 2000.
- [83] Dae-Gyu Lee, R. N. Mohapatra, M. K. Parida, and Merostar Rani. Predictions for the proton lifetime in minimal nonsupersymmetric so(10) models: An update. *Phys. Rev. D*, 51:229–235, Jan 1995.
- [84] M A Leigui de Oliveira. Expression of Interest for a Full-Scale Detector Engineering Test and Test Beam Calibration of a Single-Phase LAr TPC. Technical Report CERN-SPSC-2014-027. SPSC-EOI-011, CERN, Geneva, Oct 2014.
- [85] W. H. Lippincott, K. J. Coakley, D. Gastler, A. Hime, E. Kearns, D. N. McKinsey, J. A. Nikkel, and L. C. Stonehill. Scintillation time dependence and pulse shape discrimination in liquid argon. *Phys. Rev. C*, 78:035801, Sep 2008.
- [86] Jorge L. Lopez and Dimitri V. Nanopoulos. Flipped SU(5): Origins and recent developments. In *15th Johns Hopkins Workshop on Current Problems in Particle Theory: Particle Physics from Underground to Heaven Baltimore, Maryland, August 26-28, 1991*, pages 277–297, 1991.

- [87] Vincent Lucas and Stuart Raby. Nucleon decay in a realistic  $so(10)$  susy gut. *Phys. Rev. D*, 55:6986–7009, Jun 1997.
- [88] Ettore Majorana. Teoria simmetrica dell’elettrone e del positrone. *Il Nuovo Cimento*, 14(4):171–184, apr 1937.
- [89] Hisakazu Minakata and Alexei Yu. Smirnov. Neutrino mixing and quark-lepton complementarity. *Phys. Rev. D*, 70:073009, Oct 2004.
- [90] M. Mooney. The microboone experiment and the impact of space charge effects. 2015.
- [91] E. Morikawa, R. Reininger, P. Gürtler, V. Saile, and P. Laporte. Argon, krypton, and xenon excimer luminescence: From the dilute gas to the condensed phase. *The Journal of Chemical Physics*, 91(3):1469–1477, aug 1989.
- [92] FM Newcomer, S Tedja, R Van Berg, J Van der Spiegel, and HH Williams. A fast, low power, amplifier-shaper-discriminator for high rate straw tracking systems. *IEEE Transactions on Nuclear Science*, 40(4):630–636, 1993.
- [93] Emmy Noether. Invariant variation problems. *Transport Theory and Statistical Physics*, 1(3):186–207, jan 1971.
- [94] I. Nutini. Study of charged particles interaction processes on ar in the 0.2 - 2.0 GeV energy range through combined information from ionization free charge and scintillation light. Technical report, jan 2015.
- [95] D. R. Nygren. The time projection chamber: A new  $4\pi$  detector for charged particles. Technical report, 1974.
- [96] L. Onsager. Initial recombination of ions. *Phys. Rev.*, 54:554–557, Oct 1938.
- [97] S. Pascoli, S.T. Petcov, and A. Riotto. Leptogenesis and low energy  $cp$ -violation in neutrino physics. *Nuclear Physics B*, 774(1):1 – 52, 2007.



- 1020 [98] C. Patrignani et al. Review of Particle Physics. *Chin. Phys.*, C40(10):100001,  
1021 2016.
- 1022 [99] B. Pontecorvo. Neutrino Experiments and the Problem of Conservation of  
1023 Leptonic Charge. *Sov. Phys. JETP*, 26:984–988, 1968. [Zh. Eksp. Teor.  
1024 Fiz.53,1717(1967)].
- 1025 [100] T. Yang R. Acciarri, M. Stancari. Determination of the electron lifetime in  
1026 lariat. Technical report, March 2016.
- 1027 [101] Martti Raidal. Relation between the neutrino and quark mixing angles and  
1028 grand unification. *Phys. Rev. Lett.*, 93:161801, Oct 2004.
- 1029 [102] Steve Ritz et al. Building for Discovery: Strategic Plan for U.S. Particle Physics  
1030 in the Global Context. 2014.
- 1031 [103] C. Rubbia. The Liquid Argon Time Projection Chamber: A New Concept for  
1032 Neutrino Detectors. 1977.
- 1033 [104] L.M. Saunders. Electromagnetic production of pions from nuclei. *Nucl. Phys.*,  
1034 *B7: 293-310(1968)*.
- 1035 [105] Qaisar Shafi and Zurab Tavartkiladze. Neutrino democracy, fermion mass hier-  
1036 archies, and proton decay from 5d su(5). *Phys. Rev. D*, 67:075007, Apr 2003.
- 1037 [106] Sigma-Aldrich, P.O. Box 14508, St. Louis, MO 63178 USA.
- 1038 [107] R. K. Teague and C. J. Pings. Refractive index and the lorentz-lorenz function  
1039 for gaseous and liquid argon, including a study of the coexistence curve near the  
1040 critical state. *The Journal of Chemical Physics*, 48(11):4973–4984, jun 1968.
- 1041 [108] J. Thomas and D. A. Imel. Recombination of electron-ion pairs in liquid argon  
1042 and liquid xenon. *Phys. Rev. A*, 36:614–616, Jul 1987.

- 1043 [109] D.R.O. Morrison N. Rivoire V. Flaminio, W.G. Moorhead. Compilation of  
1044 Cross Sections I:  $\pi^+$  and  $\pi^-$  Induced Reactions. *CERN-HERA*, pages 83–01,  
1045 1983.
- 1046 [110] D.R.O. Morrison N. Rivoire V. Flaminio, W.G. Moorhead. Compilation of  
1047 Cross Sections II:  $K^+$  and  $K^-$  Induced Reactions. *CERN-HERA*, pages 83–02,  
1048 1983.
- 1049 [111] W. Walkowiak. Drift velocity of free electrons in liquid argon. *Nuclear Instru-*  
1050 *ments and Methods in Physics Research Section A: Accelerators, Spectrometers,*  
1051 *Detectors and Associated Equipment*, 449(1-2):288–294, jul 2000.
- 1052 [112] Hermann Weyl. Gravitation and the electron. *Proceedings of the National*  
1053 *Academy of Sciences of the United States of America*, 15(4):323–334, 1929.
- 1054 [113] Colin et al Wilkin. A comparison of  $\pi^+$  and  $\pi^-$  total cross-sections of light  
1055 nuclei near the 3-3 resonance. *Nucl. Phys.*, B62:61–85, 1973.
- 1056 [114] D. H. Wright and M. H. Kelsey. The Geant4 Bertini Cascade. *Nucl. Instrum.*  
1057 *Meth.*, A804:175–188, 2015.
- 1058 [115] C. S. Wu, E. Ambler, R. W. Hayward, D. D. Hoppes, and R. P. Hudson.  
1059 Experimental test of parity conservation in beta decay. *Phys. Rev.*, 105:1413–  
1060 1415, Feb 1957.
- 1061 [116] N Yahlali, L M P Fernandes, K Gonzlez, A N C Garcia, and A Soriano. Imaging  
1062 with sipms in noble-gas detectors. *Journal of Instrumentation*, 8(01):C01003,  
1063 2013.
- 1064 [117] T. Yanagida. Horizontal symmetry and masses of neutrinos. *Progress of Theo-*  
1065 *retical Physics*, 64(3):1103–1105, sep 1980.